10

SEISMIC WAVEFORM MODELING

Early in this text we stated that one of the goals of a seismologist is to understand every wiggle on the seismogram. The preceding chapters have dealt with phenomena that influence the structure of seismogram: propagation effects, source effects, and characteristics of the seismometer itself. It is possible to model each of these effects mathematically and, therefore, to develop a procedure to *predict* the character of a seismogram in a realistic model of the Earth. Such a mathematical construction is known as a *synthetic seismogram*. The formalism of comparing synthetic and observed seismograms is known as *waveform modeling*. Waveform modeling has become one of the most powerful tools available to seismologists for refining Earth structure models and understanding fault rupture processes. In general, waveform modeling is an iterative process in which differences between the observed and synthetic seismograms are minimized by adjusting the Earth structure or source representation.

The underlying mathematical theory for constructing synthetic seismograms is called *linear filter theory*. The seismogram is treated as the output of a sequence of linear filters. Each filter accounts for some aspect of the seismic source or propaga-tion. Figure 10.1 shows an example of a trapezoid-shaped *P*-wave ground displace-ment, along with recordings on short- and long-period seismometers. The trapezoid shape can be considered to be the output of filters that account for the effects of rupture on a finite fault plane as well as any propagation effects (Chapter 9). This ground motion is then distorted by the recording characteristics of the seismome-ter, a linear filter that is usually well known, and the output is a seismogram.

It is possible to characterize the ele-ments of a linear filter system by consider-ing the response of the filter to an im-pulse, or delta, function. In a physical sense, this corresponds to a single, instan-taneous pulse of energy at the source for which the complex resulting seismogram determines the propagation filter. If the impulse response of a particular filter is $f(t)$, its corresponding Fourier transform is $F(\omega)$. If $f(t)$ is known, the response, $y(t)$, of an arbitrary input, $x(t)$, can be calcu-lated with the *convolution* operator (see Box 9.2). If $X(\omega)$ is the Fourier transform of $x(t)$, then the transform of the output signal, $Y(\omega)$, is given by

$$Y(\omega) = F(\omega)X(\omega). \qquad (10.1)$$

If a signal goes through a succession of
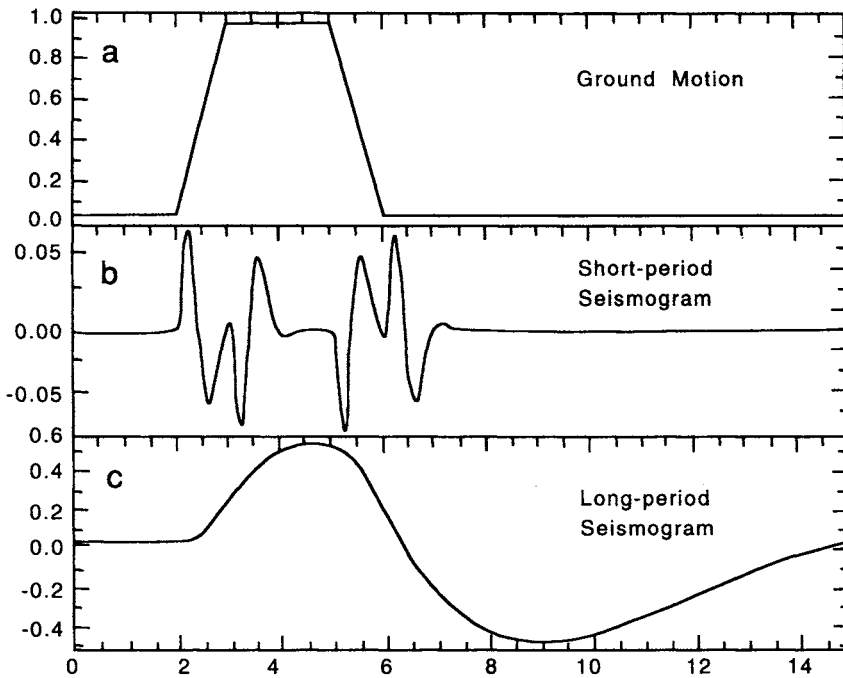
FIGURE 10.1 [Top] A trapezoid time function, corresponding to a hypothetical ground motion. (Middle) A seismogram produced by the trapezoid motion convolved with a short-period instrument response. (Bottom) A seismogram produced by the trapezoid convolved with a long-period instrument response.

filters, $f_1, f_2, \ldots f_n(t)$, the Fourier transform of the output signal is given by

$$Y(\omega) = F_1(\omega) F_2(\omega) \cdots F_n(\omega) X(\omega).$$

$$(10.2)$$

In other words, the output signal is given by the multiple product of the spectra of each filter and the input signal.

In seismic waveform modeling, there are three basic filters:

$$u(t) = s(t) * g(t) * i(t), \quad (10.3)$$

where $u(t)$ is the seismogram, $s(t)$ is the signal from the seismic source, $g(t)$ is the propagation filter, and $i(t)$ is the seismometer response. In actuality, $s(t)$ and $g(t)$ can be divided into several filters to account for specific effects. For example, $g(t)$ can be divided into a filter that accounts for the multiplicity of arrivals due to reflections and refractions at material boundaries within the Earth along with a filter that accounts for the seismic-wave attenuation. Similarly, $s(t)$ can be divided into filters accounting for source radiation conditions and fault rupture characteristics.

Linear filter theory provides a very elegant methodology for waveform modeling. It is possible to isolate the effects of one specific process on the character of the seismogram. For example, the effects of $g(t)$ for teleseismic body waves are easily accounted for, so often only the character of $s(t)$ need be adjusted or timed such that a synthetic seismogram adequately predicts an observation. Most of what is known about seismic source processes has been learned by applying such a procedure. In this chapter we will explore waveform modeling and provide some examples.

10.1 Body Waveform Modeling: The Finite Fault

We can readily construct the filters on the right-hand side of Equation (10.3) for a simple *point source*. From Figure 9.3 we know that the far-field source time history of a single particle on a fault is approximately boxcar shaped. The length of the boxcar is τ_r (the rise time), and the height of the boxcar is M_0/τ_r, where M_0 is the seismic moment. We call a single-particle fault a *point source*; the body waves from a point-source dislocation would be a simple boxcar pulse if no other filters were in operation. A more realistic source would include temporal and spatial *fault finiteness*, and the source-time function is more clearly approximated by a trapezoid (see Chapter 9). The source rise time and source finiteness can be thought of as two filters, with the output being the source-time function. Figure 10.2 shows a graphical representation of the various filters that
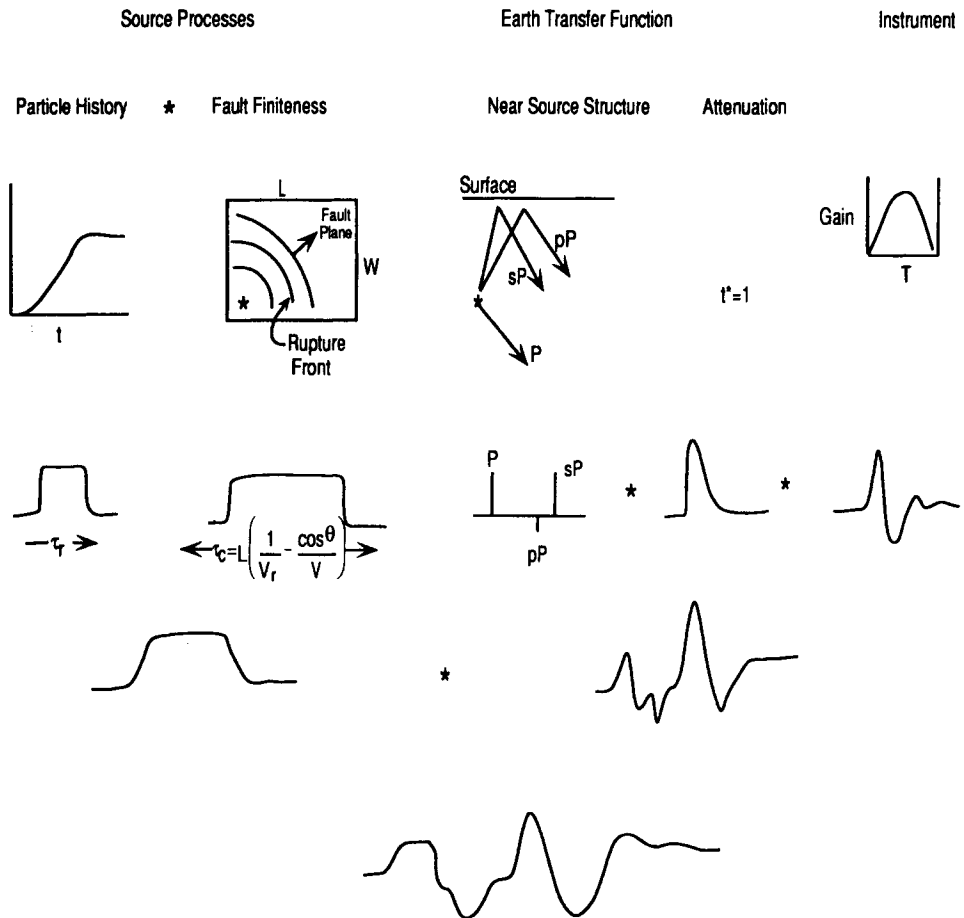
FIGURE 10.2 Schematic representation of various processes and their equivalent filter representations, which combine to give the total seismogram seen at the bottom.

produce a teleseismic body-wave seismogram, the first two of which produce the source time function.

The most complex filter in Eq. (10.3) is $g(t)$, sometimes called the *Earth transfer function*. This filter accounts for all propagation effects such as reflections, triplications, diffractions, scattering, attenuation, mode conversions, as well as geometric spreading. The usual procedure is to divide $g(t)$ into a filter that accounts for elastic phenomena, $R(t)$, and a filter that accounts for attenuation, $A(t)$. At teleseismic distances, $R(t)$ is a time series with a sequence of impulses temporally distributed to account for the variability in arrival times. At teleseismic distances, the most important P-wave arrivals are P, pP, and sP, so $R(t)$ is a "spike train" with three pulses spaced to account for the differences in arrival times. The amplitude of a given spike depends on the angle of incidence at the surface and the seismic radiation pattern. In Chapters 3 and 4, mathematical expressions were developed to calculate the amplitudes of impulse P waves. In Chapter 8, we developed the equations for a far-field P wave:

$$u_P(r,t) = \frac{1}{4\pi\rho r\alpha^3}R^P\dot{M}\left(t - \frac{r}{\alpha}\right), \quad (10.4)$$

where R^P gives the radiation pattern in terms of fault geometry and takeoff angle. We can rewrite (10.4) using the fact that any double couple can be represented as a weighted sum of three elementary faults (Section 8.5) to give

$$u_p(r,t) = \frac{1}{4\pi\rho r\alpha^3}\sum_{i=1}^{3}A_i(\phi,\lambda,\delta)c_i$$

$$* \dot{M}\left(t - \frac{r}{\alpha}\right), \quad (10.5)$$

where A_i is called the *horizontal radiation pattern* and c_i is called the *vertical radia-*

tion pattern, which are given by

$$A_1 = \sin 2\phi \cos\lambda \sin\delta$$

$$+ \tfrac{1}{2}\cos 2\phi \sin\lambda \sin 2\delta$$

$$A_2 = \cos\phi \cos\lambda \cos\delta - \sin\phi \sin\lambda \cos 2\delta$$

$$A_3 = \tfrac{1}{2}\sin\lambda \sin 2\delta, \quad (10.6)$$

where $\phi = \phi_s - \phi_f$, and

$$c_1 = -p^2$$

$$c_2 = 2\varepsilon p\eta_\alpha$$

$$\varepsilon = \begin{cases} +1 & \text{if ray is upgoing} \\ -1 & \text{if ray is downgoing.} \end{cases}$$

$$c_3 = p^2 - 2\eta_\alpha^2 \quad (10.7)$$

The three fundamental faults are (1) a vertical strike–slip fault, (2) a vertical dip–slip fault, and (3) a 45° dipping thrust fault ($\lambda = 90°$) evaluated at an azimuth of 45°. (By plugging in the appropriate strike, dip, and rake, you can see that A_2 and A_3 vanish for the first fundamental fault, A_1 and A_3 vanish for the second fundamental fault, and so on.) Equation (10.5) is extremely useful because it isolates $R(t)$ and provides a simple methodology for its calculation given an arbitrary fault orientation. If we calculate the spike train for each of the three fundamental faults, we just require a linear sum to account for the effects of any fault. Equation (10.5), as written, is only accurate for a half-space. If the P wave interacts with structure, it will undergo reflection and transmission, which depend on the angle of incidence. The c_i coefficient contains all the information about the angle, so we can rewrite (10.5) as

$$u_P(r,t) = \left(\frac{1}{4\pi\rho r\alpha^3}\sum_{k=1}^{N}\sum_{i=1}^{3}A_i c_i R_{M_{O_k}}\Pi_k\right)$$

$$* \dot{M}\left(t - \frac{r}{\alpha}\right), \quad (10.8)$$
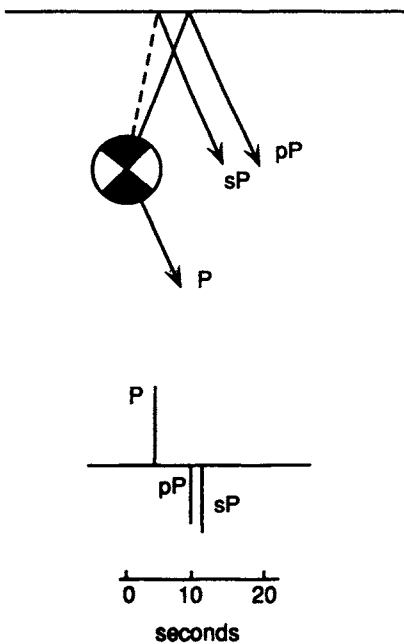
FIGURE 10.3 Primary raypaths corresponding to direct P and surface reflections pP and sP that arrive at a teleseismic station. For a shallow source these arrivals are close together in time, and together they comprise the P "arrival." The relative amplitudes of the arrivals are influenced by the source radiation pattern and the free-surface reflection coefficients. Small-amplitude differences due to extra attenuation or geometric spreading for the upgoing phases also can be accounted for if the source is deep.

where N is the number of arrivals, or rays, represented by the Earth filter; $R_{M_{O_k}}$ is the receiver function, with M being the mode type (P or S wave) of the kth ray; and O is the recording component (radial or vertical). Finally, Π_k is the product of all the transmission and reflection coefficients that the kth ray experiences on its journey from the source to receiver. The parenthetic term on the right side of Eq. (10.8) is just the $R(t)$ we need to calculate the Earth transfer function.

Although (10.8) looks complicated, it is actually straightforward to determine $R(t)$ at teleseismic distances. Figure 10.3 shows $R(t)$ for a dip–slip fault in a half-space.

The amplitudes of the depth phases are affected by both the surface reflection co-efficient and the radiation pattern from the source. In the example, P and pP both leave the source with a compressional motion. Upon reflection at the free surface, pP is inverted. The combined effects of the SV radiation pattern and free-surface reflection also invert the polarity of the sP arrival relative to P. The relative arrival times of the various phases depend on the depth of the earthquake and the distance between the source and receiver (which controls the ray parameter or take-off angle). The surface-reflection delay times are given by

$$\Delta t \approx d\eta_U + d\eta_D, \qquad (10.9)$$

where η_U and η_D are the vertical slowness of the upward and downward paths of a given depth phase and d is the hypocentral depth.

The relative amplitudes of the spikes in $R(t)$ vary greatly depending on source orientation. This variability produces waveforms that are diagnostic for different fault orientations. Waveform modeling is much more powerful for constraining fault orientation than first-motion focal mechanisms because it provides more complete coverage of the focal sphere and uses relative-amplitude information. A realistic $R(t)$ actually contains many more than just three wave arrivals. For a layered Earth structure, multiple reflections and conversions occur both near the source and beneath the receiver. In general, these multiples are much less important than the primary three rays at teleseismic distances unless the earthquake occurred beneath the ocean floor. In this case *water reverberations*, rays bouncing between the surface and ocean floor, can produce significant additional spikes.

The attenuation filter, $A(t)$, is usually represented by a t^* operator (see Chapter 3). At teleseismic distances t^* is nearly constant over much of the body-wave

frequency band and is thus easy to parameterize as a filter. Figure 3.38 shows an impulse convolved with short- and long-period instruments for several values of t^*. As t^* increases, the high frequencies are more effectively removed. Note that the *amplitude* of the short-period signal is affected by changes in t^* to a much greater degree than the long-period signal.

Figure 10.4 shows a suite of P synthetic waveforms for the relevant fundamental faults using all of the filter elements we have discussed. The corresponding Earth transfer function, which includes the radiation pattern, is given in the left-hand column, and three different time functions are used (all the sources have the same seismic moment, so the shortest-duration source has the "highest" stress drop). P and SH waveforms for different fault orientations differ enough to be diagnostic of the source type, although there are trade-offs between the various filters. Of course, much additional information is contained in the azimuthal pattern of motions that would be observed for each fundamental

fault. The source depth, time function, fault orientation, and seismic moment are known as the *seismic source parameters*. The goal of waveform modeling is to recover the source parameters by "fitting" the observed waveforms with synthetics. The strongest trade-off is between source depth and source time function duration. Figure 10.5 demonstrates this trade-off. Basically, a deeper source with a shorter-duration source function may be similar to a shallower source with a longer source function. Broadband data can overcome much of this trade-off for simple sources. However, the convolutional nature of linear filter theory implies that direct trade-offs must exist. Differences in source depth exactly trade off with complex source functions for a single station, although using multiple stations can again reduce, but not eliminate, the trade-offs.

From the mid-1970s through the early 1980s, many studies of earthquake source parameters were done using teleseismic waveform modeling, mainly of long-period WWSSN data. The methodology involved
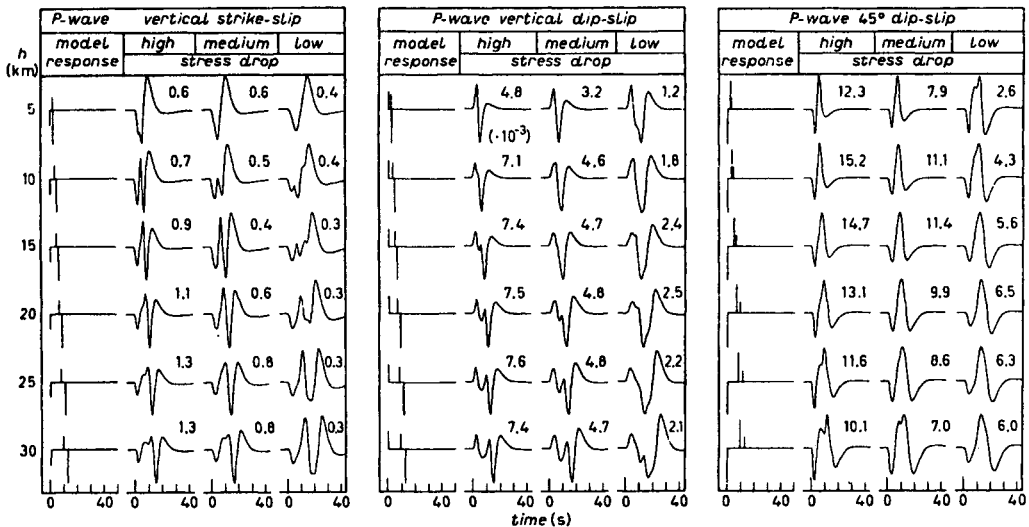
FIGURE 10.4 P-wave synthetic seismograms for the three potential terms with varying depth and time functions. The numbers in the upper right are actual potential amplitudes without the $M_0/4\pi\rho_0$, $1/R$ decay, and receiver functions included. The source time parameters, $d\tau$, are high stress drop (0.5, 1.0, 0.5), medium stress drop (1.0, 3.0, 1.0), and low stress drop (2.0, 6.0, 2.0). (From Langston and Helmberger, 1975. Reprinted with permission from the Royal Astronomical Society.)
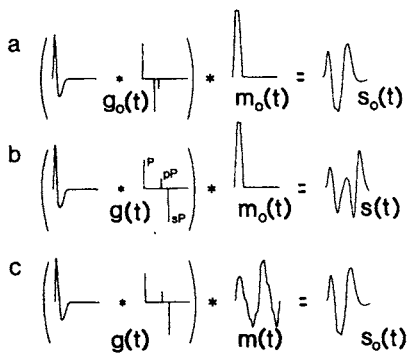
FIGURE 10.5 Illustration of the trade-off between source depth and source time function duration for teleseismic P waves. The synthetics have a long-period WWSSN response, convolved with a impulse response Green's function and a source time function. Note that identical waveforms can be produced for different combinations of Green's function and source time function (rows a and c). Both depth and mechanism were changed in this case, but simply changing depth can give the same result. The trade-offs can be overcome by using multiple stations, to some extent. (From Christensen and Ruff, 1985).

fitting long-period P and SH waves that were well distributed in azimuth about the source. The waveform information constrains the focal mechanism, depth, and source time function. A comparison of the predicted and observed *amplitudes* of the waveforms yields the seismic moment. In general, about a factor of 2 scatter is typically observed in moment estimates from station to station. This scatter reflects uncertainty in the filters, particularly $g(t)$. (Although some uncertainty was associated with the WWSSN instrument response, modern broadband digital data exhibit less amplitude scatter.) Once the time function is known, it is possible to infer the source dimensions if we assume a rupture velocity. Given an estimate of fault area, the average displacement ($\overline{D}$) on the fault and the stress drop can be calculated. Aftershock distribution or observed surface faulting is often used to estimate fault dimensions.

A fundamental concept underlying waveform modeling is separation of the source and propagation effects. For a double couple, (10.8) explicity achieves this. Now let us consider a full moment tensor source where all moment tensor terms have an identical source time history, $s(t)$. Using (8.84) we can rewrite Eq. (10.3) as

$$u_n(x,t) = s(t) * i(t) * \sum_{i=1}^{5} \left(m_i \cdot G_{in}(t) \right)$$

$$(10.10)$$

$$m_1 = M_{11}, \qquad m_2 = M_{22}, \qquad m_3 = M_{12},$$

$$m_4 = M_{13}, \qquad m_5 = M_{23},$$

where u_n is the vertical, radial, or tangential displacement, and the Earth transfer function has been replaced by the summation operator. The summation is the product of the seismic moment tensor (here represented by m_i, the five elements left when assuming no isotropic component, i.e., $m_{33} = -(m_{11} + m_{22})$, and $G_{in}(t)$, the corresponding *Green's functions*. The moment tensor terms are simply constants to be determined. The Green's functions are impulse displacement responses for a seismic source with orientation given by each corresponding moment tensor element. Note that each moment tensor Green's function i will give *three* components (n) of displacement. Any arbitrary fault orientation can be represented by a specific linear combination of moment tensor elements (see Section 8.5), so the summation in Eq. (10.10) implies that any *Earth transfer function* can also be constructed as a linear combination of Green's functions. This is an extremely powerful representation of the seismic waveform because it requires the calculation of only *five* (or with some recombination of terms, *four*) fundamental Green's functions to produce a synthetic waveform for an arbitrary moment tensor at a given distance.

Equation (10.10) is the basis .for inversion procedures to recover the seismic source parameters. It includes the purely double-couple representation in (10.8) as a

special case. In the simplest case, let us assume that the source time function and source depth are known. Then $s(t)$ and $i(t)$ can be directly convolved with the Green's functions, yielding a system of linear equations:

$$u_n(x,t) = \sum_{i=1}^{5} m_i \cdot H_{in}(t), \quad (10.11)$$

where $H_{in}(t)$ are the new Green's functions (impulse response passed through an attenuation and instrument filter). We can write (10.11) in simple matrix form

$$\mathbf{u} = \mathbf{Gm}. \quad (10.12)$$

In order to match the observed seismogram in a least-squares sense, we can draw on the methods introduced in Chapter 6 to invert (10.12) for an estimate of $\mathbf{m}$

$$\mathbf{m} = \mathbf{G}^{-1}\mathbf{u}, \quad (10.13)$$

where G^{-1} is a generalized inverse.

This holds for each time step in the observed seismogram, $u_n(x,t)$. Basically, all one is doing is find the five weighting terms (moment tensor values) of functions that add up to give the seismogram. A single horizontal record that is not naturally rotated can be used to recover the full moment tensor, because each time sample helps to constrain $\mathbf{m}$. More stable estimates of the moment tensor are provided by inverting all three components at a single station. The most stable procedure is to simultaneously fit many seismograms from stations with distinctive Green's functions. For a given time t with multiple stations (10.12) can be written in vector form as

$$\begin{bmatrix} u_1 \\ u_2 \\ \vdots \\ u_k \end{bmatrix} = \begin{bmatrix} G_{11} & G_{12} & \cdots & G_{15} \\ G_{21} & G_{22} & \cdots & G_{25} \\ \vdots & \vdots & & \vdots \\ G_{k1} & G_{k2} & \cdots & G_{k5} \end{bmatrix} \begin{bmatrix} m_1 \\ m_2 \\ \vdots \\ m_5 \end{bmatrix}$$

$$k \times 1 \qquad\qquad k \times 5 \qquad\qquad 5 \times 1,$$

$$(10.14)$$

where k is the number of waveforms of interest; when $k > 5$, the system is overdetermined, and it should be possible to resolve the moment tensor. In practice, the system must be *very* overdetermined to resolve $\mathbf{m}$, which is easily achieved using multiple time samples.

Of course, we usually do not know the source time function or source depth *a priori*, so we can recast the problem as an *iterative* inversion. In this case we discretize the source time function and invert for the time series. The two most common parameterizations of the time function are a series of boxcars, or overlapping triangles (Figure 10.6). Consider the case in which the boxcar parameterization is chosen. Then we can write $s(t)$ as

$$s(t) = \sum_{j=1}^{M} B_j b(t - \tau_j), \quad (10.15)$$

where $b(t - \tau_j)$ is equal to a boxcar of width $\Delta\tau$ that begins at time τ_j and ends at $\tau_j + \Delta\tau$, B_j is the height of the boxcar, and $M\Delta\tau$ is the total length of the time function. Equation (10.15) can be used to rewrite (10.10) as

$$u_n = i(t) * \sum_{j=1}^{M} \sum_{i=1}^{5} B_j m_i \left[b(t - \tau_j) * G_{in}(t) \right].$$

$$(10.16)$$

Now this equation has two sets of unknowns: the heights of the boxcars, B_j, and the elements of the moment tensor, m_i. Since Eq. (10.16) is a nonlinear function of the unknowns, an iterative, linearized least-squares inverse can be used. We assume an initial model, construct synthetics for it, and then match the data in a least-squares sense by minimizing the difference, $\text{obs}(t) - \text{syn}(t) = \Delta d(t)$. We then solve

$$\Delta\mathbf{d} = \mathbf{A}\,\Delta\mathbf{P}, \quad (10.17)$$

where $\mathbf{A}$ is a matrix of partial derivatives $(A_{ij} = \partial u_i / \partial P_j)$ of the synthetic waveform
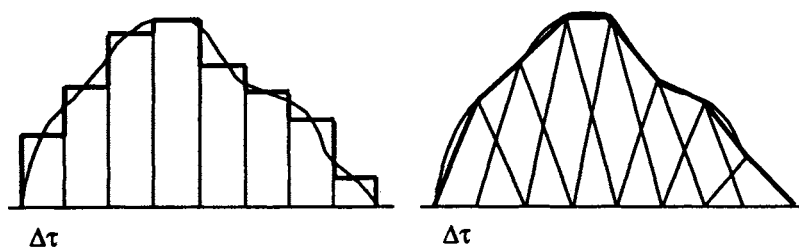
FIGURE 10.6 Two alternative parameterizations of an arbitrarily shaped source function.

(u_i) with respect to a given parameter P_j. $\Delta\mathbf{P}$ is the model vector to be solved for, which contains the *changes* in the parameters, P_j, required to diminish the difference between the observed and synthetic seismograms. This type of linearization is valid only for small $\Delta\mathbf{P}$; thus it requires a good starting model, and a criterion is added to the inversion to minimize $\Delta\mathbf{P}$.

Equation (10.17) can be solved with the generalized inverse techniques described in Section 6.4. In general, simultaneous
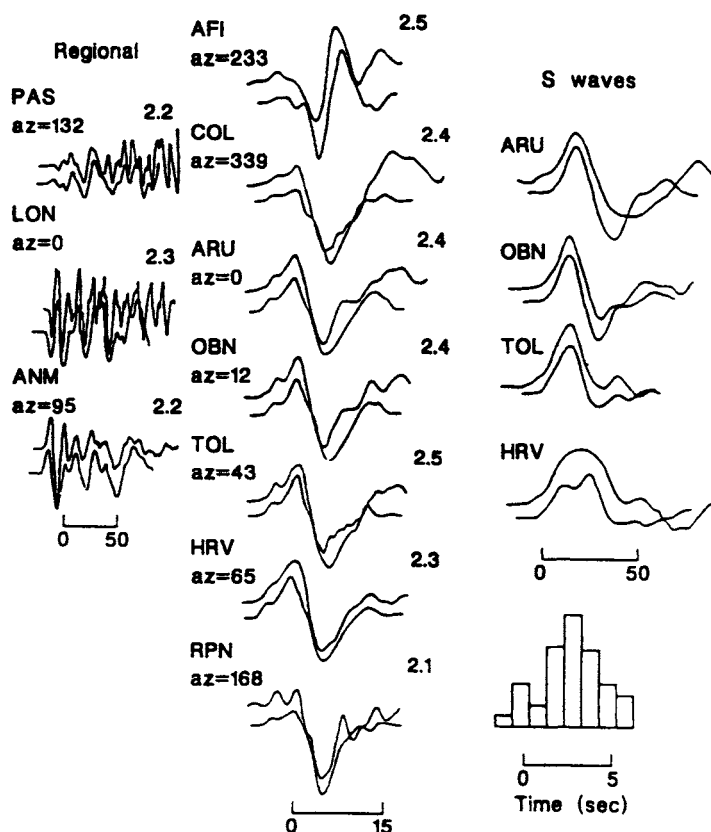

FIGURE 10.7 An example of waveform modeling for the 1989 Loma Prieta earthquake. Ground displacements are for the P_{nl} and teleseismic P and SH waves. Top trace of each seismogram pair is the observed, and bottom trace is the synthetic. The time function used is shown at the lower right. The focal mechanism determined from this inversion is $\phi_f = 128°$ $\pm 3°$, $\delta = 66° \pm 4°$, $\lambda = 133° \pm 7°$, and the moment is 2.4×10^{19} N m. (From Wallace *et al.*, 1991.)

inversion for the moment tensor constants and time function elements results in some nonlinear parameter trade-offs that can cause some singular values to be very small, but exploring the solution space by inverting with many different starting models usually yields a robust solution. The moment tensors from waveform inversion are hardly ever "perfect" double couples. The moment tensor is usually diagonalized and decomposed into a major and minor double couple or into a major double couple and a CLVD (Section 8.5 discusses these decompositions in detail). The minor double couple is usually small and is ignored; it is usually assumed that the minor double couple is the result of noise or of mapping incomplete or inaccurate Green's functions into the source parameters. Figure 10.7 shows the results of a body-wave inversion for the 1989 Loma Prieta, California, earthquake. The source time function

was parameterized in terms of boxcars. Note that it does not look like the idealized trapezoid; we will discuss source time-function complexity in Section 10.3. The moment tensor from this inversion has only a small CLVD, suggesting that representing the source as a point source double couple, with an oblique thrust focal mechanism, adequately approximates the source for teleseismic body waves.

The power of waveform modeling for determining seismic source parameters by Eq. (10.10) depends on being able to calculate the Green's functions accurately. At teleseismic distances this is usually not a problem, since the rays P, pP, and sP have simple structural interactions and turn in the lower mantle where the seismic velocity structure is smooth. Although "ringing" can occur in a sedimentary basin, for the most part teleseismic Green's functions for isolated body-wave arrivals are
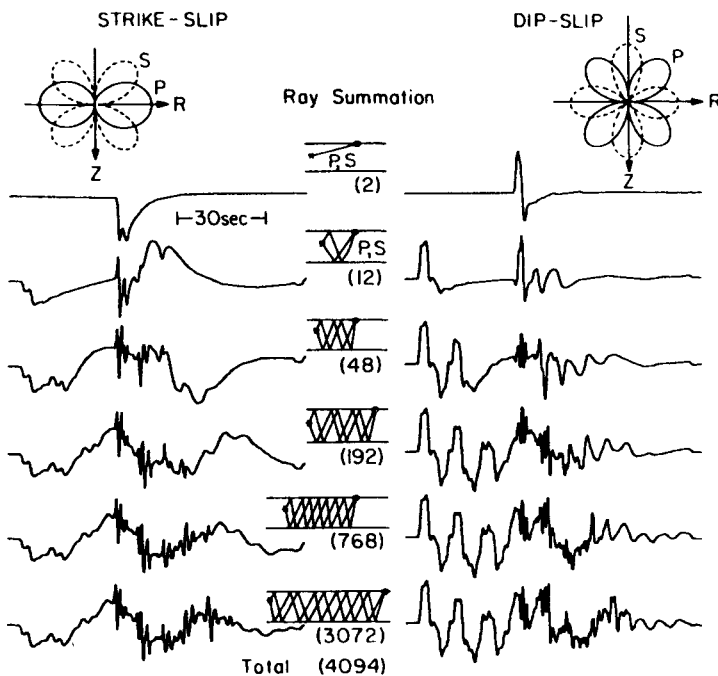
FIGURE 10.8 Vertical-component displacement seismograms for a station 1000 km from a shallow (8 km) source in a simple layer over a half-space model. No instrument response is included. (From Helmberger, 1983.)

Box 10.1 Slow Earthquakes

Although the source duration of most earthquakes scales directly with seismic moment (see Figure 9.16), there are some exceptions. In particular, *slow earthquakes* have unusually long source durations for the seismic moments associated with them. Slow earthquakes typically have an m_b that is small relative to M_s. Figure 10.B1.1 shows the effect of duration on short- and long-period body waves. The slow rise time presumably results from a very low stress drop (see Section 9.3), which controls the particle velocity. Variability in the source function occurs on all scales, from rapid events to slow creep events. Figure 10.B1.2 compares the seismic recordings of several aftershocks of the 1960 Chile earthquake. The upper two recordings are normal earthquakes, with typical fundamental mode excitation. The May 25 event has some greater complexity in the surface wave train, while the June 6 event is incredibly complex, with over an hour-long interval of surface wave excitation.

### Fault movement   Seismic waves
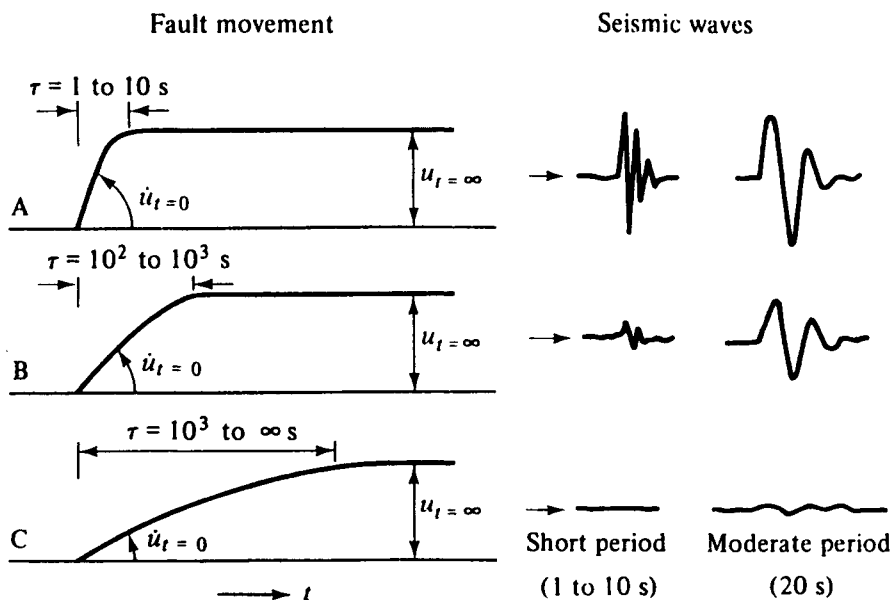
FIGURE 10.B1.1 The effect of different rise times on teleseismic signals. (From Kanamori, 1974.)

Kanamori (1972) noted that some subduction zone earthquakes produce extraordinarily large tsunamis but have moderate surface-wave amplitudes. In these cases M_S is small for the actual moment, and very slow *rupture* velocities apparently enhance the very low frequency spectrum. The physical mechanism responsible for such a slow rupture process is unknown, but in the extreme, it could produce a "silent" earthquake devoid of short-period body and surface waves. Recently, two investigators, G. Beroza and T. Jordan, suggested that several silent earthquakes

occur each year that can be identified only because they produce free oscillations of the Earth. However, several sources, including large atmospheric storms and volcanic processes, can excite low-frequency oscillations, so the source of the free oscillations observed by Beroza and Jordan is somewhat uncertain, but likely to be associated with unusual earthquake dynamics.
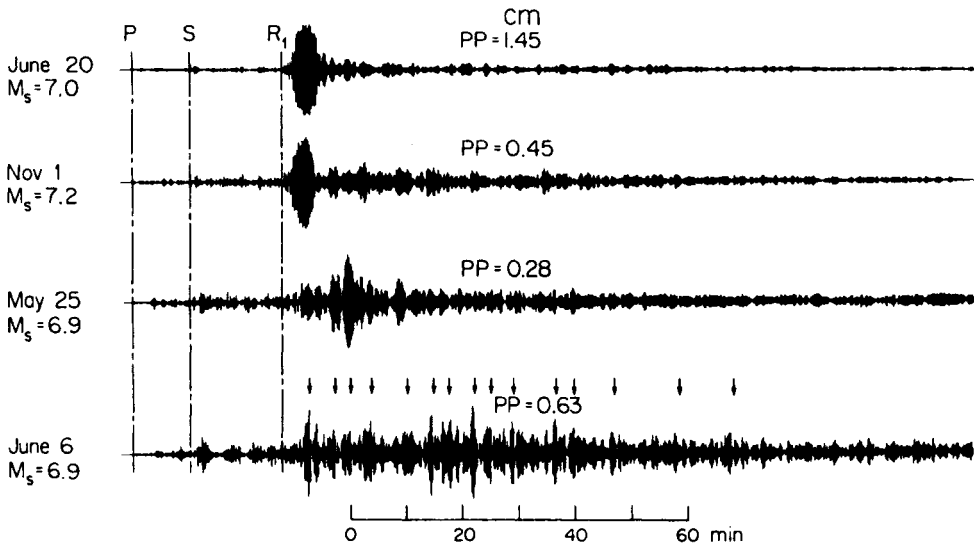

FIGURE 10.B1.2 Recordings of four aftershocks of the 1960 Chile earthquake. The upper two traces are conventional in appearance, with well-concentrated R_1 wavepackets. The lower two events have much more complex surface waves intervals, indicative of long, complex source radiation, extending over more than an hour for the June 6 event. (From Kanamori and Stewart, 1979.)

simple. This is not the case at upper-mantle and regional distances. At regional distances the crust acts as a waveguide, and hundreds of reflections between the surface and Moho are important for the waveform character. Figure 10.8 shows the vertical-component seismograms calculated for a simple layer over a half-space model for a station 1000 km from a shallow (8 km) source. Note that more than 200 rays are required before the waveform shape becomes stable. The suite of crustal reverberations following the P_n head wave comprise the P_{nl} phase. However, despite the obvious complexity in the Green's functions, the waveforms are very diagnostic of source orientation. The signature of

the seismic source on the P_{nl} waveform is robust as long as the gross parameters of the crustal waveguide (crustal thickness, average crustal seismic velocities, and upper-mantle P_n velocity) are well approximated. Figure 10.9 shows an example of inversion for source fault orientation from regional P_{nl} waveforms.

Regional-distance analysis is extremely important in the study of small or moderate-sized earthquakes ($m_b \leq 5.5$), which are rarely well recorded at teleseismic distances. Advances in broadband instrumentation have made it possible to determine the seismic source parameters from a single seismic station. The transient motion for a given double-couple orientation is
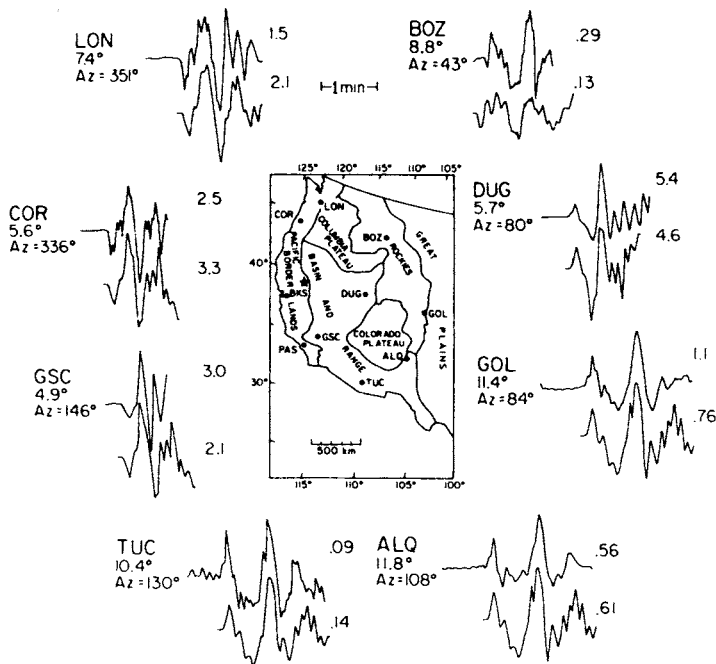
FIGURE 10.9 Comparison of regional long-period P_{nl} waveforms (upper traces) and synthetics (lower traces) obtained by waveform inversion for fault parameters of the 1966 Truckee, California, earthquake. (From Wallace and Helmberger, 1982.)

unique; thus if three components of motion are recorded, the source parameter can be determined provided that sufficiently accurate Green's functions are available (see Box 10.2).

At upper-mantle distances, triplications from the 400- and 670-km discontinuities make the body-wave Green's functions complex. Further, the mantle above the 400-km discontinuity has tremendous regional variability (Chapter 7). In general, beyond 14°, the first-arriving P wave has turned in the upper mantle, and the 400-km triplication occurs between 14° and 20°. The triplication from the 670-km discontinuity usually occurs between 16° and 23°. Figure 10.10 shows Green's functions for an upper-mantle model constructed for the western United States. The complexity and regional variability of upper-mantle-distance seismograms diminish their utility in seismic source parameter studies. Only when an earthquake occurs where the up-

per-mantle structure is very well known are the records of use for source analysis. Figure 10.11 compares observed and synthetic waveforms for the 1975 Oroville earthquake for distances from 5° to 75°, showing how well a single source model can match waveforms at regional, upper-mantle, and teleseismic distances when the structure is well known.

This text is filled with other examples of waveform modeling that have been used to illustrate various aspects of seismology. For example, Figure 9.11a shows a waveform study of the 1975 Haicheng, China, earthquake. This earthquake is well known because it was predicted by the Chinese State Seismological Bureau and the epicentral population center was evacuated, potentially saving thousands of lives. Body waves for this event show clear directivity, adding complexity to the waveforms. The pulse widths at stations to the west are much narrower than those at stations to the east,
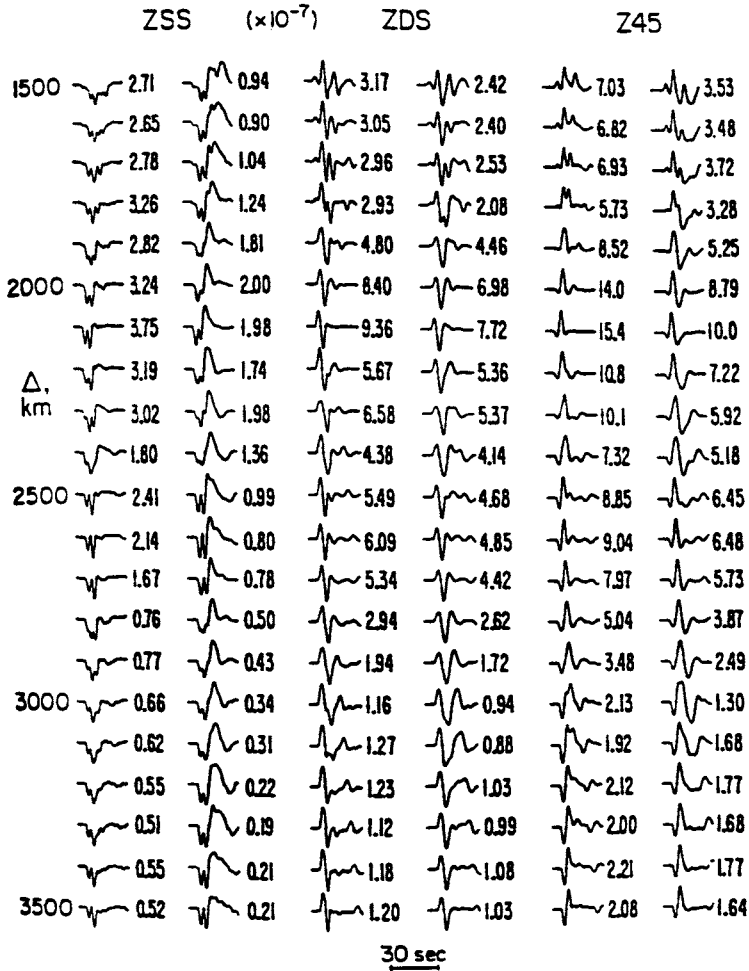
FIGURE 10.10 Upper-mantle synthetics without and with long-period WWSSN instrument for the three fundamental orientations (ZSS = vertical strike–slip; ZDS = vertical dip–slip; Z45 = 45° dip–slip at an azimuth of 45°) assuming a source depth of 8 km, $t = 1$, and $\delta t_1 = \delta t_2 = \delta t_3 = 1$ for the source time history. (Modified from Helmberger, 1983.)

Box 10.2 Source Parameters from a Single Station

In Chapter 8 we showed that slip on a fault could be represented by an equivalent double-couple force system. It turns out that the displacement field from a given double couple is *unique*, which means that if we can model the entire transient displacement field at a *single* point, we should be able to recover the source orientation. In other words, a source-parameter study should require only a
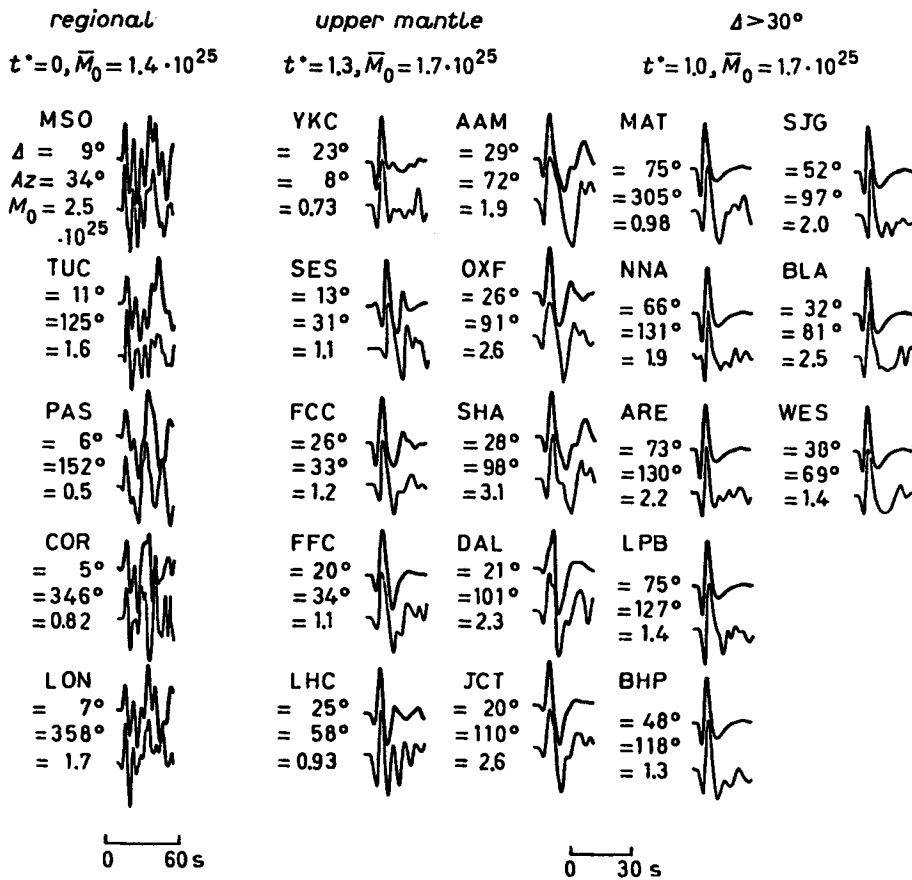
complete waveform inversion at a single seismic station. In practice, uncertainties in the Green's functions and source time function, limited bandwidth of recording instruments, and noise make this nearly impossible. However, at local and near-regional distances the effects of structure are easily accounted for, and the new generation of very broadband (vbb), high-dynamic-range instruments, such as the IRIS stations, makes it possible to use very sparse networks to determine accurately the source parameters of small to moderate-sized earthquakes.

Figure 10.B2.1 shows the recording of an $M_L = 4.9$ earthquake 12 km beneath a broadband station in Pasadena, California (PAS). The earthquake was well recorded on the Southern California network, and a first-motion focal mechanism was determined (see the second panel). The radial and tangential waveforms indicate that the source time function is complicated; for the synthetics, two triangles are assumed. The first-motion focal mechanism very poorly predicts the *SH* waveform and the relative sizes of the radial and tangential waveforms. A minor adjustment to the focal mechanism dramatically improves the quality of the fit of the synthetic to the observation. The main difference between the observed and synthetic waveforms is a *near-field* effect, not accounted for in the synthetic. This example shows the potential power of waveform inversion for complete seismograms.
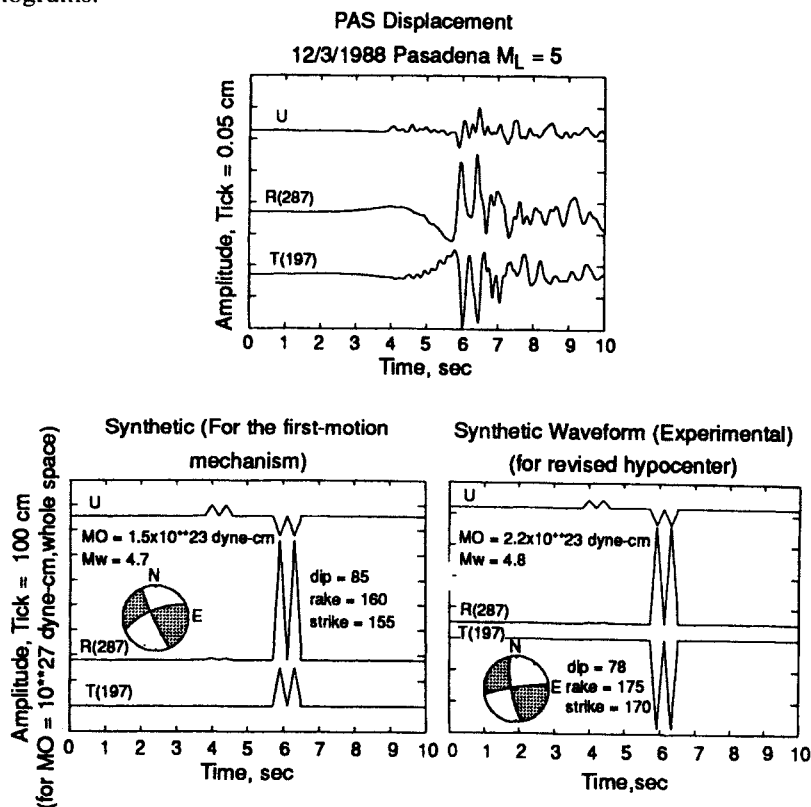
FIGURE 10.B2.1 Example of the determination of a focal mechanism by modeling the three-component data from a single station. (Modified from Kanamori *et al.*, 1990.)

regional   *upper mantle* $\Delta > 30°$

$t^* = 0, \bar{M}_0 = 1.4 \cdot 10^{25}$ $t^* = 1.3, \bar{M}_0 = 1.7 \cdot 10^{25}$ $t^* = 1.0, \bar{M}_0 = 1.7 \cdot 10^{25}$

MSO	YKC	AAM	MAT	SJG
$\Delta = 9°$	$= 23°$	$= 29°$	$= 75°$	$= 52°$
$Az = 34°$	$= 8°$	$= 72°$	$= 305°$	$= 97°$
$M_0 = 2.5$	$= 0.73$	$= 1.9$	$= 0.98$	$= 2.0$
$\cdot 10^{25}$				

TUC	SES	OXF	NNA	BLA
$= 11°$	$= 13°$	$= 26°$	$= 66°$	$= 32°$
$= 125°$	$= 31°$	$= 91°$	$= 131°$	$= 81°$
$= 1.6$	$= 1.1$	$= 2.6$	$= 1.9$	$= 2.5$

PAS	FCC	SHA	ARE	WES
$= 6°$	$= 26°$	$= 28°$	$= 73°$	$= 38°$
$= 152°$	$= 33°$	$= 98°$	$= 130°$	$= 69°$
$= 0.5$	$= 1.2$	$= 3.1$	$= 2.2$	$= 1.4$

COR	FFC	DAL	LPB
$= 5°$	$= 20°$	$= 21°$	$= 75°$
$= 346°$	$= 34°$	$= 101°$	$= 127°$
$= 0.82$	$= 1.1$	$= 2.3$	$= 1.4$

LON	LHC	JCT	BHP
$= 7°$	$= 25°$	$= 20°$	$= 48°$
$= 358°$	$= 58°$	$= 110°$	$= 118°$
$= 1.7$	$= 0.93$	$= 2.6$	$= 1.3$

|⎯⎯⎯⎯⎯|
0   60 s

|⎯⎯⎯⎯⎯|
0   30 s

FIGURE 10.11 Comparison of synthetics with waveform data for the August 1, 1975 Oroville, California, event. The preferred model is $\phi_f = 215°$, $\lambda = -65°$, and $\delta = 48°$. Inversion results: with the 5 P_{nl} records exclusively, $\phi_f = 195°$, $\lambda = -72°$, and $\delta = 46°$; with 10 upper-mantle ranges exclusively, $\phi_f = 197°$, $\lambda = -63°$, and $\delta = 58°$; with 8 teleseismic waveforms exclusively, $\phi_f = 221°$, $\lambda = 82°$, and $\delta = 44°$. (After Yao *et al.*, 1982.)

suggesting that the fault ruptured westward along the nodal plane striking 288°. (This strike is consistent with the surface trace of the fault and the aftershock distribution.) Figure 9.11 shows the observed variability in the time function plotted as a function of azimuth, as well as a theoretical model for a fault propagating to the west for 22 km at a velocity of 3.2 km/s. The synthetic seismograms shown in Figure 9.11 were generated with directivity built into the time function.

The methodology described for inverting body waves for seismic source parameters can be applied as soon as a waveform is "extracted" from a seismogram. Recently, the IRIS Data Management System has developed dial-up access to a significant part of the GSN (see Chapter 5). IRIS uses this remote access to implement a data-gathering system known as spyder™. When an earthquake occurs, it is located by the NEIC (National Earthquake Information Center), and an electronic message is broadcast to IRIS. The spyder system then calls GSN stations and downloads broadband seismic waveforms. These waveforms are then available via Internet to any interested seismologist. In practice, data from any earthquake greater

than magnitude 6.5 are available within several hours. Thus it is possible to recover seismic source parameters within a matter of hours for large events anywhere in the world. Recent developments have made it possible to trigger spyder even more rapidly for regional networks, such as that in the western United States. It is now possible to determine focal mechanisms and seismic moments for western U.S. earthquakes with $M > 4.5$ within 1 h. This "near-real-time" analysis is used to identify the causal fault, to anticipate ensuing tsunami hazard, and to predict where strong shaking is likely to have occurred to assist in emergency response activities or shutdown of critical lifelines such as freeways and train tracks.

10.2 Surface-Wave Modeling for the Seismic Source

In Section 8.6 we discussed how fault orientation could be constrained from amplitude and phase of surface waves. It is possible to invert this information to determine the moment tensor from surface waves, but the *resolving* power for source depth and source time function is intrinsically limited. The amplitude and phase of a Rayleigh or Love wave is very dependent on the velocity structure along the travel path. This means that we must correct for the effects of velocity and attenuation heterogeneity precisely for an inversion scheme to be robust. This is equivalent to knowing the Earth transfer function in body-wave inversion procedures, but there we are not as sensitive to absolute travel time as we are for surface waves. This usually means that surface-wave inversions are best performed at very long periods (> 100 s) for which the heterogeneity is relatively well mapped. These periods are so long compared to most source durations that we can usually consider the far-field time function simply as a boxcar function

with duration τ. In this case we can write the source *spectrum* of an earthquake source as

$$V(\omega, h, \phi) = \alpha(\omega, h, \phi) + i\beta(\omega, h, \phi),$$
(10.18)

where ω is frequency, h is source depth, and ϕ is the takeoff azimuth. For Rayleigh waves the real (α) and imaginary (β) parts of the spectrum are

$$\alpha = -P_R(\omega, h) M_{12} \sin 2\phi$$

$$+ \tfrac{1}{2} P_R(\omega, h)(M_{22} - M_{11}) \cos 2\phi$$

$$- \tfrac{1}{2} S_R(\omega, h)(M_{22} + M_{11}) \quad (10.19a)$$

$$\beta = Q_R(\omega, h) M_{23} \sin \phi$$

$$+ Q_R(\omega, h) M_{13} \cos \phi \quad (10.19b)$$

and for Love waves

$$\alpha = -\tfrac{1}{2} P_L(\omega, h)(M_{22} - M_{11}) \sin 2\phi$$

$$- P_L(\omega, h) M_{12} \cos 2\phi \quad (10.20a)$$

$$\beta = -Q_L(\omega, h) M_{13} \sin \phi$$

$$+ Q_L(\omega, h) M_{23} \cos \phi. \quad (10.20b)$$

The P_R, S_R, Q_R, P_L, and Q_L terms are called *surface-wave excitation functions* (analogous to the body-wave Green's functions) and depend on the elastic properties of the source region and the source depth. Figure 10.12 shows P_L as a function of depth and period for different types of travel paths.

The spectrum, V, is calculated directly from the surface-wave seismogram if that seismogram has been corrected for instrument response and propagation effects. We can rewrite (10.18) as a matrix equation. For example, for Rayleigh waves

$$\mathbf{V} = \mathbf{BD}, \quad (10.21)$$

where

$$V = \begin{bmatrix} \alpha \\ \beta \end{bmatrix} \qquad (10.22)$$

$$B = \begin{bmatrix} -\sin 2\phi & \frac{1}{2}\cos 2\phi & -\frac{1}{2} & 0 & 0 \\ 0 & 0 & 0 & \sin\phi & \cos\phi \end{bmatrix}$$

$$(10.23)$$

$$D = \begin{bmatrix} P_R M_{12} \\ P_R(M_{22} - M_{11}) \\ S_R(M_{11} + M_{22}) \\ Q_R M_{23} \\ Q_R M_{13} \end{bmatrix}. \qquad (10.24)$$

Now **B** is a known matrix, depending only on source–receiver geometry; thus **D** contains all the unknowns. Equation (10.21) can be extended to the spectra observed at N stations. Then **B** is a $2N \times 5$ real matrix, and **V** is a real vector with dimension $2N$. This system of equations can be solved for $\mathbf{D}(\omega)$ at several frequencies. Typically the optimal choice of source duration τ is determined as that which minimizes the misfit in this inversion.

Once **D** has been determined, it is possible to decompose it into two vectors, one

containing the excitation functions and the other containing the elements of the moment tensor:

$$\Lambda = \left[D^T(\omega_1), D^T(\omega_2), \ldots, D^T(\omega)_n \right]^T$$

$$\Lambda = \mathbf{EM}, \qquad (10.25)$$

where

$$E = [E_1, E_2, \ldots, E_n]^T$$

$$E_i = \mathrm{diag}[P_R(\omega_i), P_R(\omega_i), S_R(\omega_i),$$

$$Q_R(\omega_i), Q_R(\omega_i)]$$

$$M = [M_{12}, M_{22} - M_{11}, M_{22}$$

$$+ M_{11}, M_{23}, M_{13}]^T. \qquad (10.26)$$

Equation (10.25) is a standard overdetermined problem that can be solved by least squares. For any real data, there will be some misfit to the spectrum, which can be measured as *error*. The excitation functions in E_i are, of course, dependent on depth, so the inversion must be repeated for several depths. A comparison of the
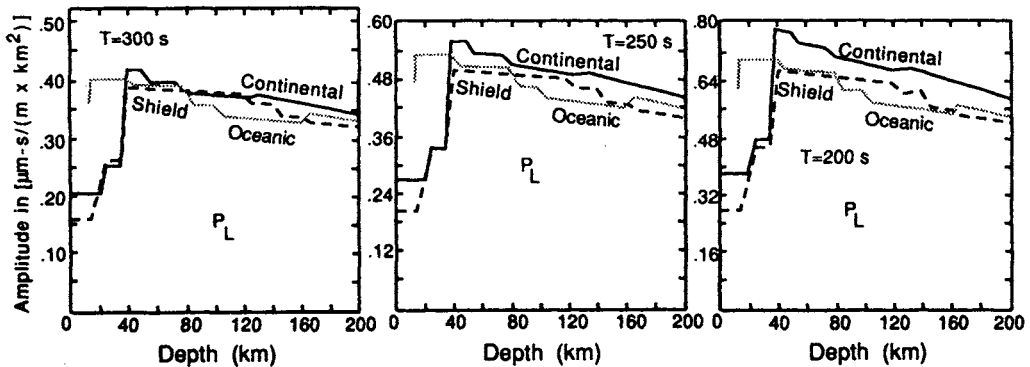
FIGURE 10.12 Dependence of the fundamental Love-mode displacement spectrum on source depth for a vertical strike–slip source. Excitation functions are shown for three different upper-mantle models, representative of shield, continental, and oceanic regions. Variations in the excitation coefficients as a function of period provide information about the source depth. (From Ben Menahem and Singh, 1981.)

errors for the different depths should result in a *minimum error*, which yields the source depth and thus the preferred moment tensor.

Let us return to the question of the source time function. We stated that the *details* of the time function do not affect the spectrum much. This is true to the extent that the source can be approximated as a point source with a boxcar source function. For large events the effective source duration will have an azimuthal pattern, as can be seen by considering the equation for source finiteness (9.20). Directivity effects are more apparent in surface waves than in body waves because their phase velocity is much slower. This source finiteness not only causes an azimuthal pattern in the phase but also reduces the amplitude of short-period waves; thus the spectrum for a large event must be corrected for source finiteness.

Figure 10.13 shows a series of moment tensor estimates from inversions of long-period surface-wave spectra (Figure 8.30) from the 1989 Loma Prieta earthquake. Several combinations of global attenuation models and source region excitation structures are considered. These inversions

Box 10.3 Centroid Moment Tensor Solutions

In 1981 the seismology research group at Harvard headed by Adam Dziewonski began routinely determining the seismic source parameters of all earthquakes with $M_s \geq 5.5$ using the centroid moment tensor (CMT) method. This inversion process simultaneously fits two signals: (1) the very long period ($T > 40$ s) body wave train from the P-wave arrival until the onset of the fundamental modes and (2) mantle waves ($T > 135$ s). These are fit for the best point-source hypocentral parameters (epicentral coordinates, depth and origin time) and the six independent moment tensor elements (not assuming a deviatoric source). The CMT solves an equation very similar to (10.10):

$$u_n(x,t) = \sum_{i=1}^{6} \psi_{in}(x,x_s,t) \cdot m_i, \qquad (10.2.1)$$

where ψ_{in} is called the *excitation kernel* and is essentially the complete seismogram Green's function for each of the moment tensor elements. The receiver is at x, and the source is at x_s (which is unknown). One initially estimates m_i, and then an iterative procedure begins that adjusts both the location and source orientation to minimize

$$u_n - u_n^0 = a_n \delta r_s + b_n \delta \theta_s + c_n \delta \phi_s + d_n \delta t_s + \sum_{i=1}^{6} \psi_{in}^0 \cdot \delta m_i, \qquad (10.2.2)$$

where u_n^0 and ψ_{in}^0 are based on the initial estimate. δr_s, $\delta \theta_s$, and $\delta \phi_s$ are the changes in spatial coordinates of the hypocenter, and a_n, b_n, and c_n are the partial derivatives with respect to perturbations in the hypocentral coordinates. δt_s is the change in the origin time. The kernels are obtained by summing the normal modes of the Earth. Thus the excitations exist *a priori*, and the inversion process can be efficiently performed for many events. Figure 10.B3.1 shows the Harvard CMT catalogue for the month of July 1990. The moment tensors are not constrained to be double couples; hence many focal mechanisms are shaped more like baseballs (large CLVD components) than the expected sectioned beach balls (double couples). The largest earthquake during this month was the July 24, 1990 Philippines event (see also Figure 1.15 for more CMT solutions).
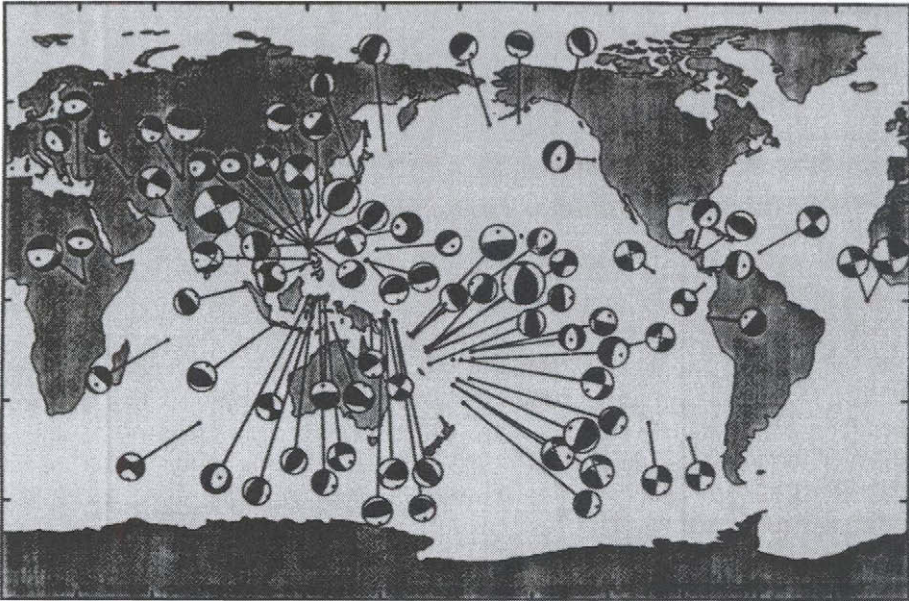
**FIGURE 10.B3.1** Harvard CMT solutions for the month of July, 1990. (Based on Dziewonski *et al.*, 1991.)

provide insight into trade-offs associated with specifying source velocity and Q models. In all cases the major double couple is nearly identical to that determined from the body waveform inversion, but the minor double-couple component varies from 3% to 14% for different Earth models. This leads to a word of caution about comparing source parameters determined for different wave types. Various seismic waves are sensitive to different aspects of the rupture process, and it is *very* important to note that path corrections and the choice of attenuation will significantly affect source depths determined from surface-wave inversions. Surface waves can

better constrain total seismic moment and total rupture duration than shorter-period waves can.

10.3 The Source Time Function and Fault Slip

Thus far in our discussion of faulting and radiated seismic energy, we have assumed that the rupture process is fairly smooth. This predicts a simple far-field time function approximated by a trapezoid, and slip is described by $\overline{D}$ (the average slip). In detail, the actual slip on a fault is not smoothly distributed, and source time functions deviate significantly from trapezoids. For example, consider the time function for the Loma Prieta earthquake in Figure 10.7. The irregularity of the time function is the result of temporally and spatially heterogeneous slip on the fault. Figure 10.14 shows the inferred variation in slip magnitude along the fault plane of the Loma Prieta earthquake. This slip function was derived by waveform modeling of both teleseismic P and SH waves and strong motion records from areas close to the fault. The slip is concentrated in two patches, with relatively small slip in the intervening regions. The regions of very high slip, known as asperities, are extremely important in earthquake hazard analysis because the failure of the asperities radiates most of the high-frequency seismic energy. The concentration of slip on asperities implies they are regions of high moment release, which, in turn, implies a fundamental difference in the fault behavior at the asperity compared with that of the surrounding fault. A conversion of slip to stress drop indicates that asperities are apparently regions of high strength (very large stress drop). The reason for the high relative strength could be heterogeneity in the frictional strength of the fault contact or variations in geometric orientation of the fault plane.
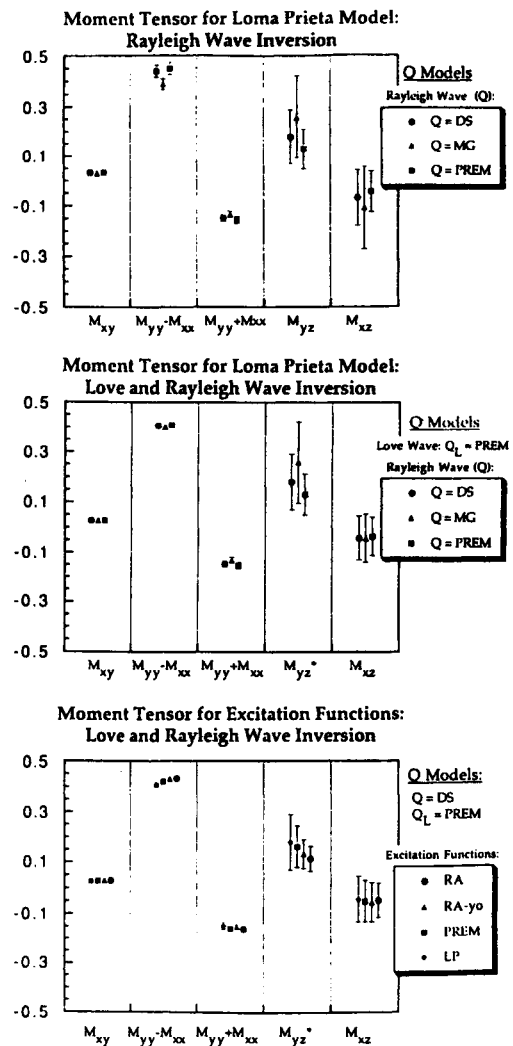
FIGURE 10.13 Moment tensor elements (Kanamori notation—see Box 8.3) for the Loma Prieta earthquake estimated from long-period Rayleigh- and Love-wave spectral inversions. Results are shown for several different attenuation models and for excitation functions from different Earth structures. (From Wallace et al., 1991.)

The geometric explanation for asperities reflects the fact that faults are not perfectly planar. On all scales, faults are rough and contain jogs or steps. The orientation of the fault plane as a whole is driven by the regional stress pattern. Segments of
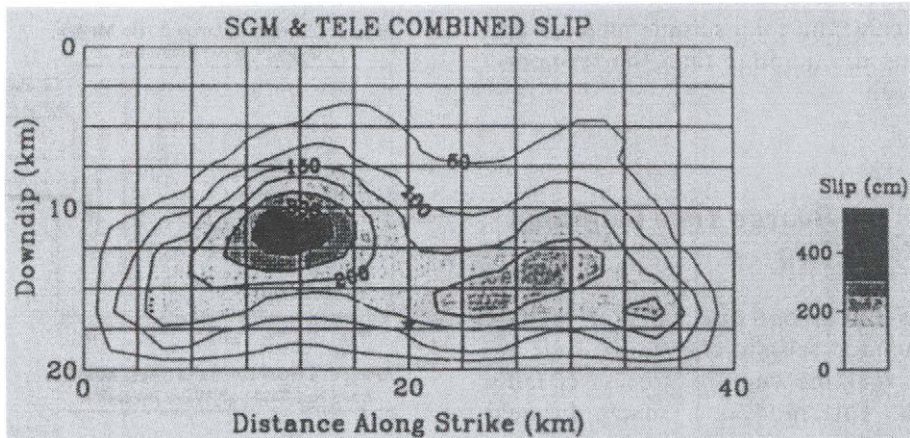
FIGURE 10.14 Slip distribution on the fault associated with the 1989 Loma Prieta earth-quake (NW end on the fault on the left). There are two prominent regions of slip, known as asperities. (From Wald *et al.*, *1991.*)

Box 10.4 Tectonic Release from Underground Nuclear Explosions

Theoretically, the seismic waves generated by an underground nuclear explosion should be very different from those generated by an earthquake. An explosive source creates an isotropic stress imbalance without the shear motion that characterizes double-couple sources. Therefore, the seismograms from an explosion should not have *SH* or Love waves, but as we saw in Figure 8.B1.1, many explosions do have *SH*-type energy. This energy is thought to be generated by a "tectonic" component, namely the release of preexisting strain by the detonation of an explosion. There are three possible mechanisms for generation of the nonisotropic seismic radiation, known as *tectonic release*: (1) triggering of slip on prestressed faults, (2) release of the tectonic strain energy stored in a volume surrounding the explosion, and (3) forced motion on joints and fractures. For all three of these mechanisms for tectonic release, the long-period teleseismic radiation pattern can be represented by an equivalent double-couple source. Depending on the orientation and size of the tectonic release, the seismic waveforms from underground explosions can be significantly modified from those we expect for an isotropic source (an explosion).

Waveform modeling can be used to constrain the size and orientation of the tectonic release. For large explosions, it appears that tectonic release is associated with a volume of material surrounding the detonation point, and the volume is related to the size of the explosion. If an explosion is detonated within the "volume" of a previous explosion, the tectonic release is dramatically reduced. Figure 10.B4.1 shows two large underground nuclear explosions at the Nevada Test Site (NTS). BOXCAR (April 26, 1968, $m_b = 6.2$) was detonated 7 yr before COLBY (March 14, 1975, $m_b = 6.2$); the epicenters are separated by less than

3 km. Although the *P* waveforms recorded at LUB are similar, there are some distinct differences. Below the BOXCAR waveform is a synthetic seismogram constructed by "adding" the waveform of a strike–slip earthquake to the waveform of COLBY. The near-perfect match between the observed and synthetic waveform for BOXCAR supports the double-couple interpretation for tectonic release.
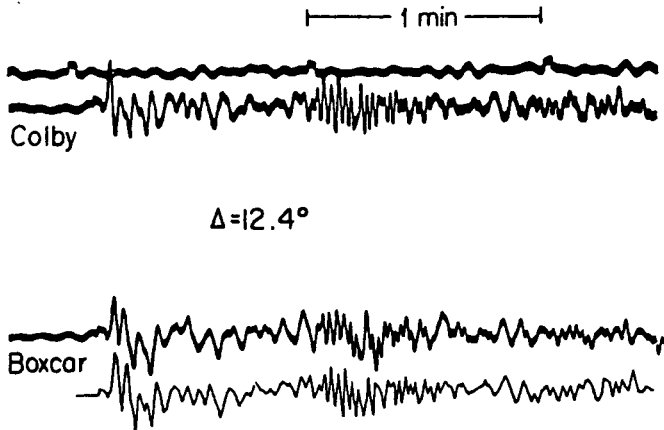
FIGURE 10.B4.1 A comparison of the *P* and P_L waveforms for BOXCAR and COLBY at LUB. Also shown is a synthetic waveform constructed by summing the COLBY waveform and a synthetic calculated for a strike–slip double couple (moment is 1.0×10^{17} N m). (From Wallace *et al.*, 1983.)

the fault that are subparallel to this orientation can have significantly higher normal stresses than surrounding regions, making them "sticking" points that resist steady, regular slip. Figure 10.15 shows a geometric irregularity that could serve as an asperity. The size and apparent strength of the asperity depend on d_s and θ_s (see Figure 10.15). At high frequencies, failure of discrete asperities may be manifested as distinct seismic arrivals. This implies that the details of source time functions may correspond to seismic radiation on particular segments of the fault. Figure 10.16 shows the source time function and inferred fault geometry for the 1978 Santa Barbara, California, earthquake (m_b = 5.8). The short-period *P* waves for this oblique thrust event are more complex than the long-period *P* waves. This results from the passband of the instrumentation,

which consists of WWSSN long- and short-period (1-s) seismometers, as illustrated in Figure 10.1. The long-period instrument cannot resolve the double peak apparent in the short-period signals, and the short-period records do not record the longer-period slip associated with the entire fault. The spatial distribution and orientation of the two asperities were determined from strong-ground-motion recordings. The new generation of very broadband seismometers has reduced the need for operating numerous instruments at a site to recover the details of faulting, and seismologists have begun to produce *unified source models*, which can be used to explain the entire faulting process from static offset to 10 Hz. These source models may include variation in the slip direction on the fault as well as variation in the slip magnitude. For the Loma Prieta event,
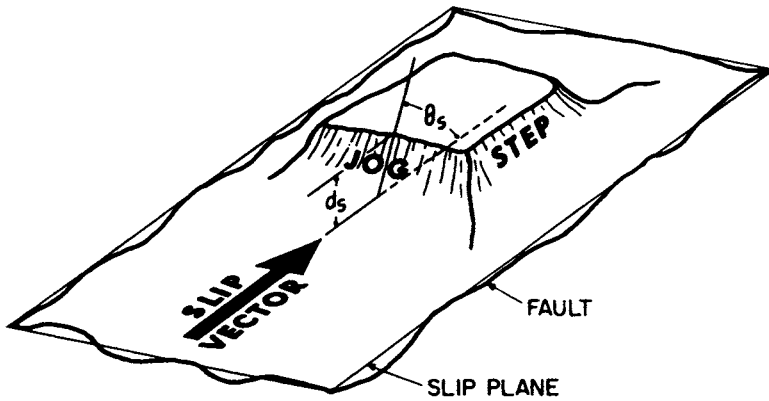
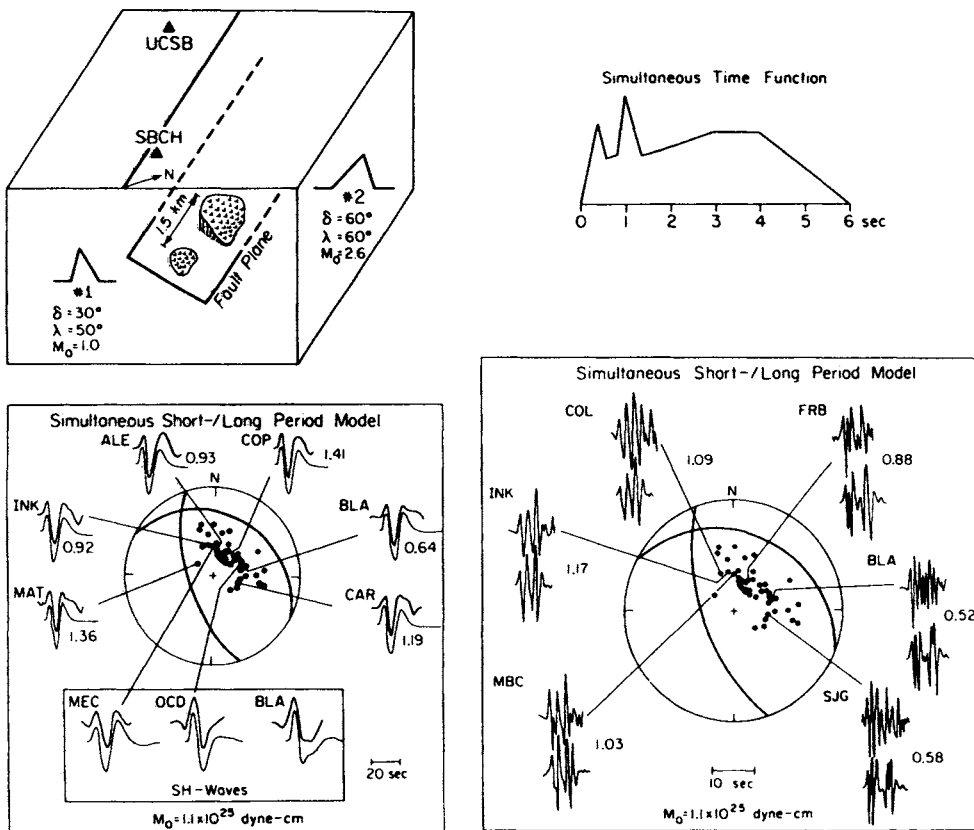**FIGURE 10.15** Geometric irregularity that could serve as an asperity. (From Scholz, 1990.)

FIGURE 10.16 Source time function and inferred fault geometry for the 1978 Santa Barbara, California, earthquake (m_b =5.8). (From Wallace et al., 1981.)

Figure 1.7 shows a model of variable slip on the fault from both local and teleseismic signals.

In general, there are no near-field recordings for most earthquakes of interest, and we must infer any faulting heterogeneity from details of the far-field time function alone. As discussed in Section 10.1, the source time function is usually determined iteratively in generalized source-parameter inversion. Another approach is to recast Eq. (10.10) as a *deconvolution* problem

$$u_n(x,t)*(g(t)*i(t))^{-1} = s(t) \quad (10.27)$$

or

$$\frac{u(\omega)}{g(\omega)i(\omega)} = s(\omega). \quad (10.28)$$

This deconvolution procedure is a natural extension of linear filter theory. This is possible when the source orientation is known independently and we simply want the source time function. The major problem with this procedure is that it maps uncertainty in the Earth transfer function and source orientation into the time function. This is a problem for analysis of large earthquakes unless the Earth transfer function correctly includes the effects of fault finiteness. One way to allow for finiteness is to produce a suite of Earth transfer functions for a given geometry and write the time-domain displacement response as

$$u(x,t) = \sum_{j=1}^{M} B_j[b(t-\tau_j)*g_j], \quad (10.29)$$

where g_j is the Earth transfer function from the jth element of the fault that "turns on" at some time τ_j, which is prescribed by the rupture velocity; $b(t-\tau_j)$ is the parameterization of the time function as described in Eq. (10.15); and B_j is the variable of interest in the inversion, namely the strength of element $b(t-\tau_j)$ in the

source time function. A separate source time function is found for each element of the fault by solving for $B_j(t)$. Figure 10.17 shows an example of the forward problem for a fault that ruptures from 15 to 36 km depth. It is obvious that unless the variability in timing of the depth phases is accounted for, an inversion for the time function will be biased. Figure 10.18 shows examples of inversions for source time function based on Eq. (10.29).

The time functions in Figure 10.18 indicate very different fault behavior. The Solomon Islands earthquake had a much smoother source process than the Tokachi–Oki earthquake. The bursts of moment release during the Tokachi–Oki earthquake suggest that several asperities along the fault plane broke when the rupture front arrived. This type of time-function variability has been used to characterize segments of subduction zones. Figure 10.19 shows the source time functions from four great subduction zone earthquakes and a model for the distribution of asperities in different subduction zones. In the case of subduction zones, the variability of asperity size and distribution presumably reflects *coupling* between the subducting and overriding plates. The Aleutian subduction zone is strongly coupled along the segment that generated the 1964 Alaskan earthquake, and the Kuril region is characterized by weaker coupling and sporadic asperity distribution. The factors causing the variability in coupling are discussed in the next chapter, but the asperity model suggests that an earthquake in a strongly coupled region would be much larger than in a weakly coupled subduction zone. We will discuss coupling in much greater detail in Chapter 11.

Let us return to the heterogeneity of slip on the fault plane as shown in Figure 10.14. An important question is, What causes the rupture to stop? Along with the concept of asperities, the concept of *barriers* has been introduced for regions on the fault that have exceptional strength and
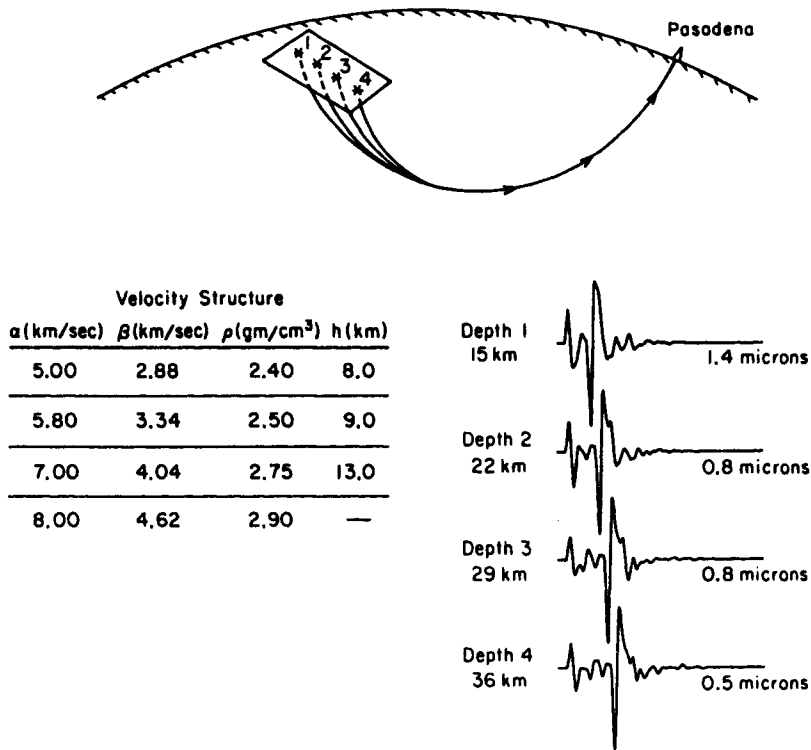
FIGURE 10.17 Earth transfer functions for a four-point source representation of a thrusting earthquake. The sum of the $g(t)$ convolved with time functions appropriate for each point source will give the synthetic seismogram. (From Hartzell and Heaton, 1985.)

impede or terminate rupture. Alternatively, barriers may be regions of low strength in which the rupture "dies out." This type of barrier is known as a *relaxation barrier*. The concepts of strength and relaxation barrier are generally consistent with the asperity model if adjacent segments of the fault are considered. A strength barrier that terminates rupture from an earthquake on one segment of the fault may serve as an asperity for a future earthquake. Similarly, the high-slip region of a fault during an earthquake may act as a relaxation barrier for subsequent earthquakes on adjacent segments of the fault. Aseismic creep may also produce relaxation barriers surrounding asperities that limit the rupture dimensions when the asperity fails. Unfortunately, there are also inconsistencies between the barrier and

asperity models of fault behavior. In Figure 10.14 a region of moderate slip is located between the two asperities. Is this reduced slip caused by a region of previous failure, or is this a region of the fault that is primed for a future earthquake? It may be possible to resolve this question by studying the detailed spatial distribution of aftershocks. If the regions adjacent to the asperities have a concentration of aftershocks but the asperities themselves are aftershock-free, this would be inconsistent with strength barriers. There is some indication that aftershock distributions outline asperities, but there are still problems with spatial resolution that preclude strong conclusions. Aftershocks are clearly a process of relaxing stress concentrations introduced by the rupture of the mainshock, but there remains an active debate as to
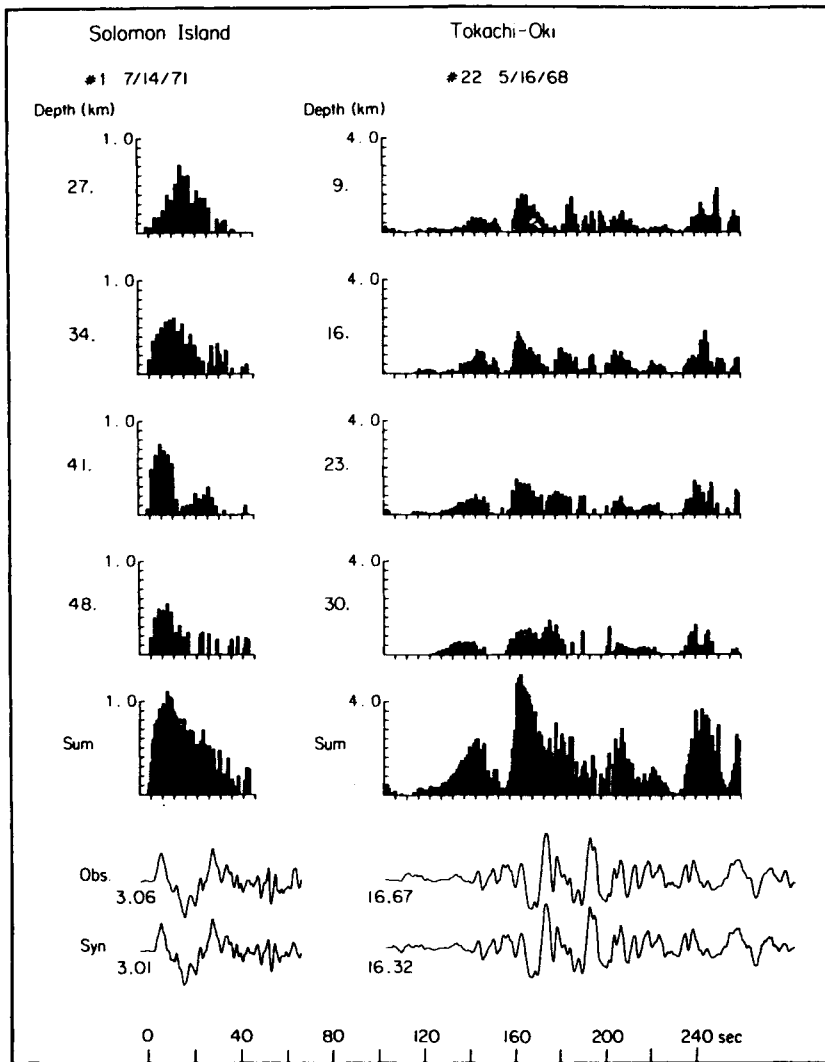
FIGURE 10.18 The source time function for two subduction zone earthquakes. Separate time functions are shown for each point source at four depths, with a sum being shown above the observed and synthetic seismograms. (From Hartzell and Heaton, 1985.)

their significance in terms of asperities and barriers. The only thing that is certain is that, averaged over long periods of time, the entire fault must slip equal amounts.

10.4 Complex Earthquakes

Fault roughness and the asperity model appear to apply to earthquakes at all scales.

When earthquakes reach a certain size, the faulting heterogeneity can be represented with the concept of *subevents*. In other words, for some large events the seismic source process can be thought of as a series of moderate-sized earthquakes. When source time functions become sufficiently complicated to suggest earthquake multiplicity, the event is known as a *complex earthquake*. Because all earthquakes
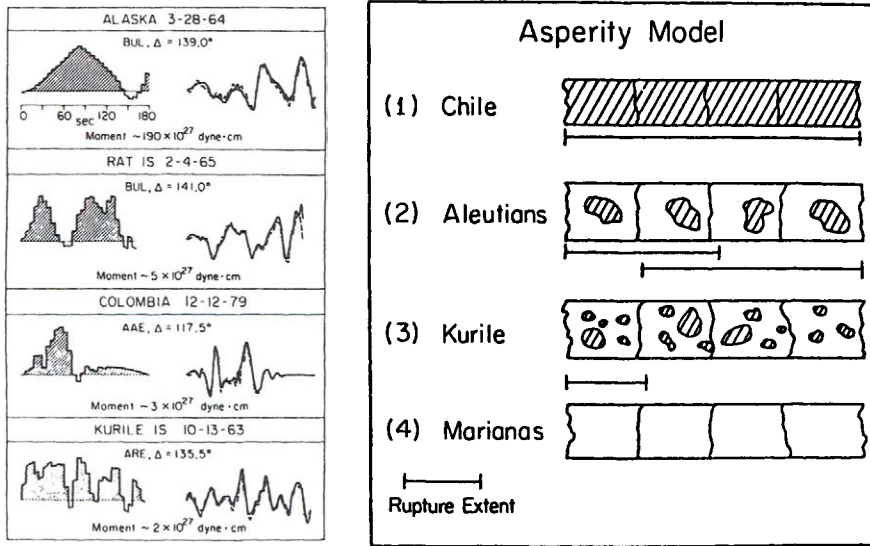
FIGURE 10.19 Source time functions from four great subduction zone earthquakes and a model for the distribution of asperities in different subduction zones. (Left is from Ruff and Kanamori, 1983; right is from Lay and Kanamori, 1981.)

## Box 10.5 Modeling Tsunami Waveforms for Earthquake Source Parameters

In Chapter 4 we discussed the propagation of tsunamis, which were generated by rapid displacement of the ocean floor during the faulting process. Just as the seismic recording of a surface wave is a combination of source and propagation effects, the tidal gauge recordings of a tsunami are sensitive to the slip distribution on a fault and the ocean bathymetry along the travel path. It is possible to invert the waveform of a tsunami (ocean height as a function of time) for fault slip. The propagation effects are easily modeled because the tsunami velocity depends only on the water depth, which is usually well known. Figure 10.B5.1 shows the observed and synthetic tsunami waves from the 1968 Tokachi–Oki earthquake, which was located northeast of Honshu, Japan. Figure 10.B5.2 compares the fault slip derived from the inversion of the tidal gauge data and that determined by the analysis of surface waves. The general agreement between both models is good; slip is concentrated west and north of the epicenter (arrows on figures), while slip south of the epicenter was zero or very small.

The inversion of tsunami data is potentially very useful for pre-WWSSN data. Few high-quality seismic records exist to estimate the heterogeneous fault motion of these older events, but older tidal gauge records often exist that are as good as modern records.
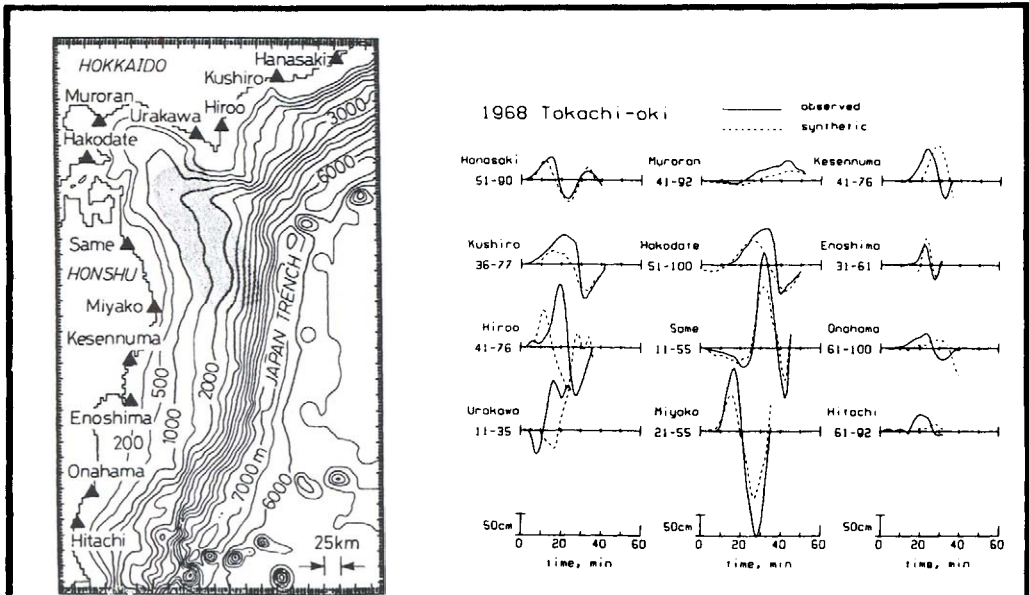
FIGURE 10.B5.1 Comparison between observed and predicted tsunamis for the 1968 Tokachi–Oki earthquake. The model fault is rectangular with heterogeneous slip. (From Satake, *J. Geophys. Res.* **94**, 5627–5636, 1989; © copyright by the American Geophysical Union.)
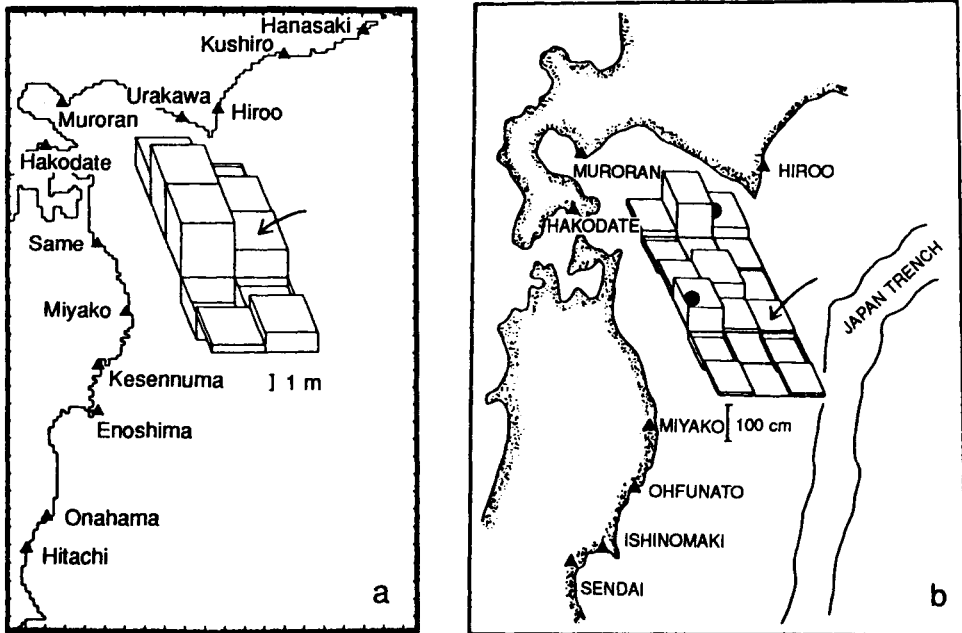
FIGURE 10.B5.2 Fault slip inferred from (a) tsunami data and (b) seismic surface waves. (From Satake, *J. Geophys. Res.* **94**, 5627–5636, 1989; © copyright by the American Geophysical Union.)
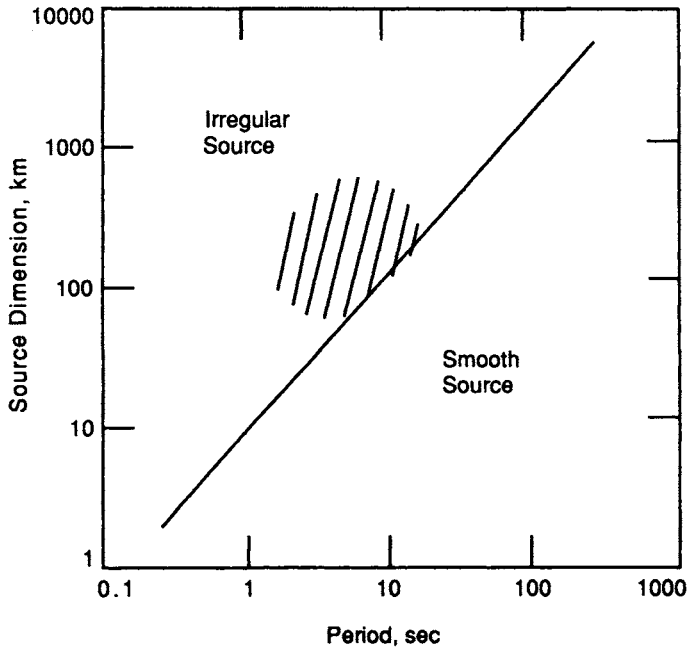
FIGURE 10.20 Empirical classification of complex earthquakes. (After H. Kanamori.)
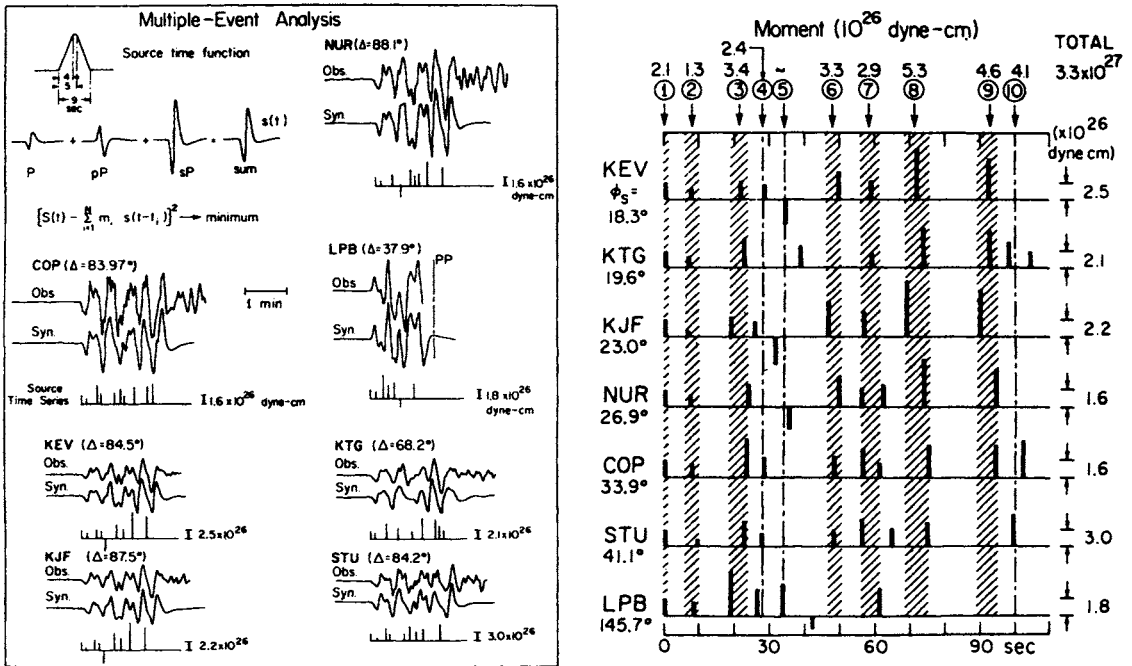

FIGURE 10.21 Multiple shock analysis for the February 4, 1976 Guatemala earthquake. (From Kanamori and Stewart, *J. Geophys. Res.* **83**, 3427–3434, 1978; © Copyright by the American Geophysical Union.)

are complex in detail, we usually reference fault complexity to the passband of observation. Figure 10.20 is an empirical classification of complex earthquakes; in the period band 5–20 s, many earthquakes with source dimensions that are greater than 100 km are complex. This is particularly true for strike–slip earthquakes. Figure 10.21 shows a multiple shock analysis for the February 4, 1976 Guatemala earthquake. A sequence of subevents is used to match each complex waveform, with consistency between the station sequences indicating the rupture complexity. The strike–slip rupture propagated bilaterally away from subevent 1, radiating pulses of energy as each fault segment failed. In this analysis it is assumed that each subevent has a specified fault orientation (the fault curves from west to east; see Figure 1.16). By matching the observed waveforms at stations azimuthally distributed around the source, we can determine the timing and moment of each subevent.

In our previous discussion of inverting for source parameters, we assumed that the rupture front progressed in a smooth and predictable manner. Clearly, in the case of the Guatemalan earthquake we have no *a priori* constraints that the rupture is smooth, nor should we expect it to be bilateral. It is possible to develop a generalized waveform inversion in which the *temporal* and *spatial* distribution of moment release can be recovered. In the simplest case, a fault can be parameterized as a series of subevents with known spatial coordinates but with unknown moment release or rupture time. Then the least-squares difference between an observed waveform and a synthetic is given by

$$\Delta = \int_0^\infty \left[u(t) - mw(t - t_1) \right]^2 dt, \quad (10.30)$$

where $u(t)$ is the observed seismogram, w is a synthetic seismogram calculated for a point source [w is given by (10.3), with $s(t)$, the appropriate time function for a

"unit" earthquake of moment m_0]. m is the size scaling factor, and Δ is minimized in terms of m and t_1; thus the timing and size of a subevent can be determined. We can generalize Eq. (10.30) to many subevents and multiple observations by successively "stripping away" the contribution of each subevent. In this procedure a wavelet is fit to the data, and a residual waveform is used to define a new seismogram. This residual is fit with another wavelet, stripped, and so on until the entire observed seismogram is adequately explained. This problem is usually severely underdetermined, so a "search procedure" is used to find the minima in Δ. The generalized form of (10.30) is given by

$$\Delta_k = \sum_{j=1}^M \int \left[x_{jk}(t) - m_k w_{jk}(t - \tau_k, f_k) \right]^2 dt,$$

$$(10.31)$$

where M is the number of stations used, x_{jk} is the residual data at the jth station after $k - 1$ iterations, m_k is the moment chosen for the kth iteration, w_{jk} is the synthetic wavelet for the jth station from the kth subevent, τ_k is the timing of the kth subevent, and f_k gives the source parameters for the kth subevent (epicenter, focal mechanism, etc.). The spatial–temporal resolution of a given subevent can be evaluated by plotting the correlation between the observed waveform and the synthetic wavelet at various allowable fault and time locations. Figure 10.22 shows the correlation for *three* iterations of such an inversion for the Guatemala earthquake. t is the time after rupture began, and l is the distance along the fault from the epicenter. For the first iteration the correlation is highest at a time of approximately 20 s and a distance of 90 km *west* of the epicenter. After this subevent is stripped away (removing the *largest* moment subevent), the process is repeated, and the largest correlation is 60 s from rupture
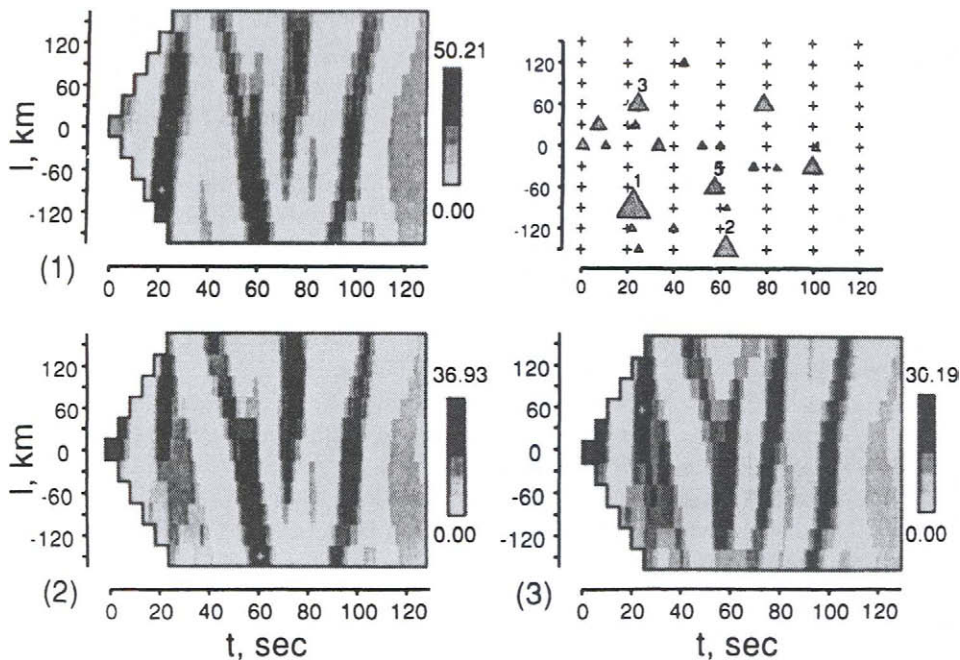
FIGURE 10.22 Correlation for three iterations of inversion for the Guatemala earthquake. The darker values indicate times and locations in which point sources can explain power in the residual seismogram from the previous iteration. The upper right shows the space–time sequence of pulses, with the size of triangles indicating the relative moment of pulses along the fault. (From Young *et al.*, 1989.)

initiation, 150 km west of the epicenter. This process is repeated for a prescribed number of iterations, and the results from each iteration are combined to give the overall rupture process. It is interesting to note that the largest moment release for the Guatemala earthquake occurred near the bend in the Motagua fault, consistent with our discussion earlier in this chapter about asperities produced by irregularities.

The procedure described above has been extended to invert for source orientation of various subevents. Figure 1.16 shows corresponding results for the Guatemala earthquake with variable subevent fault orientation and moment being recovered. Such an application has a huge number of parameters and is reliable only with an extensive broadband data set.

Another waveform-modeling procedure to recover temporal changes in fault orien-

tation is to invert for a *time-dependent* moment tensor. In this case we can rewrite Eq. (10.10) as

$$u_n(x,t) = \sum_{i=1}^{5} m_i(t) * G_{in}(x,t), \quad (10.32)$$

where now the moment tensor elements are independent time series of moment release, and we incorporate the instrument response in the Green's function. Each moment tensor element now has its own time history, or time function. In the frequency domain we can write this as

$$u_n(x,\omega) = \sum_{i=1}^{5} m_i(\omega) G_{in}(x,\omega), \quad (10.33)$$

where m_i is the only unknown and it is a set of constants for each *frequency*. We can solve for m_i at a set of discrete fre-

quency points and use the inverse Fourier transform to obtain a time-dependent moment tensor. In matrix form, Eq. (10.33) for a single frequency, f, looks like

where u_1^R and u_1^I correspond to the observed spectra at station 1 at frequency f, and u_n^R and u_n^I correspond to the spectra at station n at frequency f. The Green's

$$
\begin{bmatrix} u_1^R \\ u_1^I \\ \vdots \\ u_n^R \\ u_n^I \end{bmatrix} = \begin{bmatrix} G_{11}^R & -G_{11}^I & & G_{15}^R & -G_{15}^I \\ & & \cdots & & \\ G_{11}^I & G_{11}^R & & G_{15}^I & G_{15}^R \\ \vdots & \vdots & \ddots & \vdots & \vdots \\ G_{n1}^R & -G_{n1}^I & & G_{n5}^R & -G_{n5}^I \\ & & \cdots & & \\ G_{n1}^I & G_{n1}^R & & G_{n5}^I & G_{n5}^R \end{bmatrix} \begin{bmatrix} m_1^R \\ m_1^I \\ \vdots \\ m_5^R \\ m_5^I \end{bmatrix}, \quad (10.34)
$$

Box 10.6 Empirical Green's Functions

Although Earth models have become quite sophisticated, there are many instances where our ability to compute accurate theoretical Green's functions is inadequate to allow source information to be retrieved from particular signals. This is very common for broadband recordings of secondary body waves with complex paths in the Earth (*PP*, *SSS*, etc.), as well as for short-period surface waves ($T = 5$–80 s). A strategy for exploiting these signals is to let the Earth itself calibrate the propagation effects for these signals, which are usually very complex. This is achieved by considering seismic recordings from a small earthquake located near a larger event of interest. If the source depth and focal mechanism of the two events are identical, the Earth response to each station will be the same. If the small event has a short, simple (impulse-like) source time function, its recordings approximate the Earth's Green's functions, including attenuation, propagation, instrument, and radiation pattern effects, with a corresponding seismic moment. We use these signals to model the signals for a larger event, with the differences being attributed to the greater complexity of the source time function for the larger earthquake. Often this involves deconvolving the "empirical" Green's functions from the corresponding records for the larger event. This provides an approximation of the source time function for the larger event, normalized by the seismic moment of the smaller event (Figure 10.B6.1). Isolated phases with a single ray parameter are usually deconvolved, with azimuthal and ray parameter (takeoff angle) variations in the relative source time functions providing directivity patterns that allow finiteness of the larger event to be studied. The procedure is valid for frequencies below the corner frequency of the smaller event, and in practice it is desirable to have two orders of magnitude difference in the seismic moments. Rupture processes of both tiny and great events have been studied in this way.
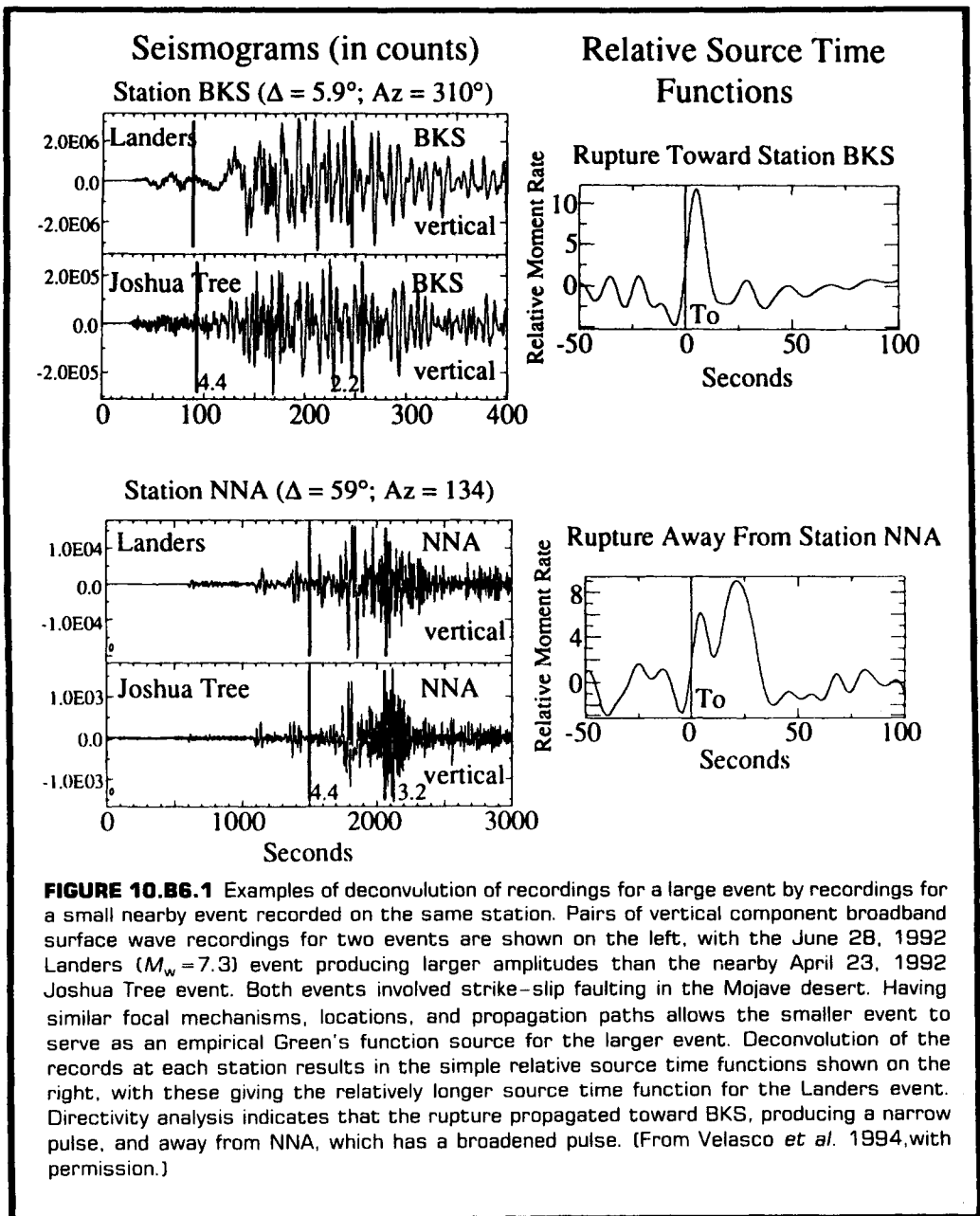
FIGURE 10.B6.1 Examples of deconvolution of recordings for a large event by recordings for a small nearby event recorded on the same station. Pairs of vertical component broadband surface wave recordings for two events are shown on the left, with the June 28, 1992 Landers (M_w =7.3) event producing larger amplitudes than the nearby April 23, 1992 Joshua Tree event. Both events involved strike-slip faulting in the Mojave desert. Having similar focal mechanisms, locations, and propagation paths allows the smaller event to serve as an empirical Green's function source for the larger event. Deconvolution of the records at each station results in the simple relative source time functions shown on the right, with these giving the relatively longer source time function for the Landers event. Directivity analysis indicates that the rupture propagated toward BKS, producing a narrow pulse, and away from NNA, which has a broadened pulse. (From Velasco *et al.* 1994,with permission.)

function matrix is composed of 10 columns corresponding to the real and imaginary parts of five moment tensor elements for each station. This is required because of the complex multiplication: $(m^R + m^I)(G^R + G^I)$. The real part is $(m^R G^R - m^I G^I)$, and the imaginary part is $(m^R G^I + m^I G^R)$.

Inversion of (10.34) is typically unstable at high frequencies due to inaccuracies of the Green's functions, so only the lower frequencies are used. Figure 10.23 shows the results of a time-dependent moment-tensor inversion for the 1952 Kern County earthquake. The results show a temporal evolu-
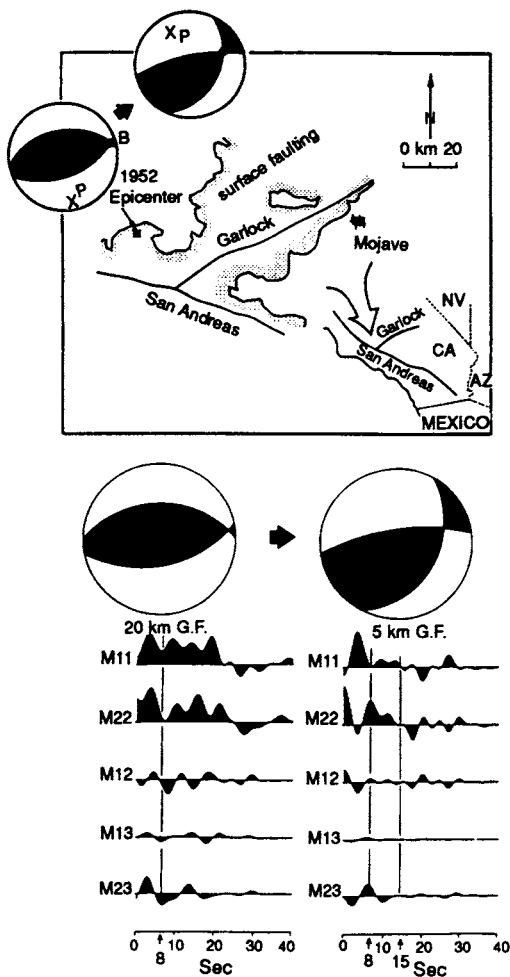
FIGURE 10.23 Results of a time-dependent moment-tensor inversion of the 1952 Kern County earthquake. Source time functions for each moment tensor element are shown for two depths. The preferred solution involves a pure thrust at 20 km depth in the first 8 s and a shallower oblique component in the next 7 s.

tion of rupture from primarily northwest–southeast thrusting to east–west oblique strike–slip motion. The geologic interpretation of the Kern County earthquake is that it started at the southwest corner of the fault at a depth of approximately 20 km. The fault ruptured to the northeast, where the fault plane became much shallower and the slip became partitioned into shortening (thrusting) and strike–slip com-

ponents. For the entire rupture, the P axes remained nearly constant, but the T axis rotated from being nearly vertical to a much more horizontal position.

## 10.5 Very Broadband Seismic Source Models

As the preceding discussions have indicated, seismologists use numerous methodologies to extract the details of faulting from seismic waveforms. We have tried to cast these different procedures in the context of linear filters and have concentrated on recovering the source time function. The one filter element we have largely ignored is the instrument response. This is because it is well known and can often be removed from the problem, but limited instrument bandwidth does provide an important constraint on our ability to recover source information. Given that earthquakes involve faulting with a finite spatial and temporal extent, different-frequency waves are sensitive to different characteristics of the rupture process. Further, different wave types tend to have different dominant observable frequencies as a result of interference during rupture and propagation. The net result is that wave types recorded on band-limited instruments can resolve different aspects of the fault history. Thus, inversion of the body-wave recording on WWSSN instruments may give a different picture of an earthquake than inversion of very long period surface waves recorded on a gravimeter. A truly broadband source model is required to explain rupture over a frequency range of a few hertz to static offsets. The new generation of broadband instruments help tremendously toward this end, but part of the problem is intrinsic to the physics of the seismic-wave generation. For example, the broadband waves from the 1989 Loma Prieta earthquake can be used to resolve two asperities. The funda-

mental-mode Rayleigh-wave analysis cannot resolve these details, but it does provide an accurate estimate of the total seismic moment. This moment is 20–30% larger than that determined by the body waves; thus the body waves are missing some of the slip process, perhaps a component of slow slip.

An ideal seismic source inversion would *simultaneously* fit the observations from different wave types over a broad frequency range. In practice, the methodology has been to perform distinct, high-resolution inversion of each wave type, thus solving for the source characteristics best resolved by a particular wave type. The distinct source characteristics are then merged to give a total model of the source. When incompatibilities in source characteristics determined by different inversions are observed, *ad hoc* procedures are used to merge the source characteristics. For example, consider the moment discrepancy for the Loma Prieta earthquake. Figure 10.24 shows the effect of adding a long-period component of moment to the derived body-wave time function for Loma Prieta. Note that the "slow slip" component does not noticeably affect the body waves if it is spread out over more than 30 s. Although the slip model would account for the observed body and surface waves, it would require a type of fault behavior that is not observed in the laboratory. Given the uncertainty in various model assumptions, it is often difficult to judge how far to interpret these complex models from merging of results for different wave types.

A major problem with simply combining all different wave types in a single inversion is the normalization of the data. How does one weight a misfit in a P waveform as compared to a misfit of a single spectral
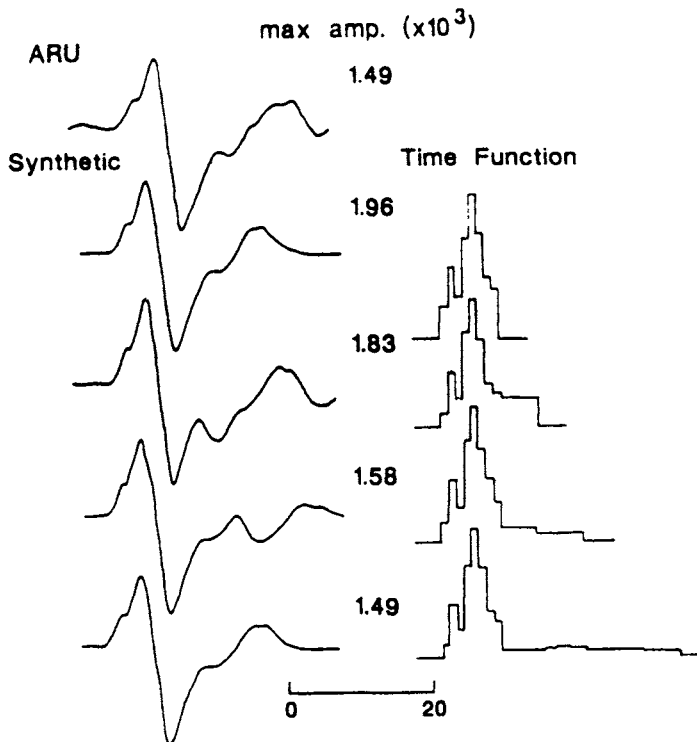
FIGURE 10.24 Effect of adding a long-period component of moment to the derived body-wave time function for the Loma Prieta earthquake. (From Wallace *et al.*, 1991.)

point for a long-period surface wave? Currently, strategies for deriving very broadband source models include iterative *feedback* inversions in which the body waves, high-resolution surface waves, and near-field strong motions are inverted independently. The results from each inversion are combined into a new starting model, which is, in turn, used in a heavily damped repeat of the independent inversions. After several iterations, all the data are combined, and the misfit is measured by a single error function, which is minimized in a final inversion. This type of procedure improves the *ad hoc* model merging and results in a model that is consistent with the sampled range of the seismic spectrum. Ultimately, it will be desirable to achieve this routinely, but this will require a better understanding of model dependence for different wave analyses.

References

Ben Menahem, A., and Singh, S. J. (1981). "Seismic Waves and Sources." 1108 pp. Springer-Verlag, New York.

Christensen, D. H., and Ruff, L. J. (1985). Analysis of the trade-off between depth and source time functions. *Bull. Seismol. Soc. Am.* **75**, 1637–1656.

Dziewonski, A. M., Ekström, G., Woodhouse, J. H., and Zwart, G. (1991). Centroid-moment tensor solutions for July–September, 1990. *Phys. Earth Planet. Inter.* **67**, 211–220.

Hartzell, S. H., and Heaton, T. H. (1985). Teleseismic time functions for large, shallow subduction zone earthquakes. *Bull. Seismol. Soc. Am.* **75**, 965–1004.

Helmberger, D. V. (1983). Theory and application of synthetic seismograms. *In* "Earthquakes: Observation, Theory and Interpretation," pp. 174–222. Soc. Ital. Fis., Bologna.

Kanamori, H. (1972). Mechanism of tsunami earthquakes. *Phys. Earth Planet. Inter.* **6**, 346–359.

Kanamori, H. (1974). A new view of earthquakes. *In* "Physics of the Earth (A Modern View of the Earth)" (in Japanese), pp. 261–282. (H. Kanamori and E. Boschi eds.), Physical Society of Japan, Maruzen, Tokyo.

Kanamori, H., and Stewart, G. S. (1978). Seismological aspects of the Guatemala earthquake of February 4, 1976. *J. Geophys. Res.* **83**, 3427–3434.

Kanamori, H., and Stewart, G. S. (1979). A slow earthquake. *Phys. Earth Planet. Inter.* **18**, 167–175.

Kanamori, H., Mori, J., and Heaton, T. H. (1990). The 3 December 1988 Pasadena earthquake ($M_L = 4.9$) recorded with the very broadband system in Pasadena. *Bull. Seismol. Soc. Am.* **80**, 483–487.

Langston, C. A., and Helmberger, D. V. (1975). A procedure for modeling shallow dislocation sources. *Geophys. J. R. Astron. Soc.* **42**, 117–130.

Lay, T., and Kanamori, H. (1981). An asperity model of large earthquake sequences. *Maurice Ewing Ser.* **4**, 579–592.

Ruff, L., and Kanamori, H. (1983). The rupture process and asperity distribution of three great earthquakes from long-period diffracted *P*-waves. *Phys. Earth Planet. Inter.* **31**, 202–230.

Satake, K. (1989). Inversion of tsunami waveforms for the estimation of heterogeneous fault motion of large submarine earthquakes: The 1968 Tokachi–Oki and 1983 Japan Sea earthquakes. *J. Geophys. Res.* **94**, 5627–5636.

Scholz, C. H. (1990). "The Mechanics of Earthquakes and Faulting." Cambridge Univ. Press, Cambridge, UK.

Velasco, A. A., Ammon, C. J., and Lay, T. (1994). Empirical Green function deconvolution of broadband surface waves: Rupture directivity of the 1992 Landers California ($m_w = 7.3$) earthquake. *Bull. Seismol. Soc. Am.* **84**, 735–750.

Wald, D. J., Helmberger, D. V., and Heaton, T. H. (1991). Rupture model of the 1989 Loma Prieta earthquake from the inversion of strong-motion and broadband teleseismic data. *Bull. Seismol. Soc. Am.* **81**, 1540–1572.

Wallace, T. C., and Helmberger, D. V. (1982). Determining source parameters of moderate-size earthquakes from regional waveform. *Phys. Earth Planet. Inter.* **30**, 185–196.

Wallace, T. C., Helmberger, D. V., and Ebel, J. E. (1981). A broadband study of the 13 August 1978 Santa Barbara earthquake. *Bull. Seismol. Soc. Am.* **71**, 1701–1718.

Wallace, T. C., Helmberger, D. V., and Engen, G. R. (1983). Evidence of tectonic release from underground nuclear explosions in long-period *P* waves. *Bull. Seismol. Soc. Am.* **73**, 593–613.

Wallace, T. C., Velasco, A., Zhang, J., and Lay, T. (1991). A broadband seismological investigation of the 1989 Loma Prieta, California, earthquake: Evidence for deep slow slip? *Bull. Seismol. Soc. Am.* **81**, 1622–1646.

Yao, Z. X., Wallace, T. C., and Helmberger, D. V. (1982). Earthquake source parameters from sparse body wave observations. *Earthquake Notes* **53**, 38.

Young, C. J., Lay, T., and Lynnes, C. S. (1989). Rupture of the 4 February 1976 Guatemalan earthquake. *Bull. Seismol. Soc. Am.* **79**, 670–689.